Single neurons and networks in the claustrum integrate input from widespread cortical sources

Andrew M. Shelton[1,✉], David K. Oliver[1], Joachim S. Grimstvedt[2], Ivan P. Lazarte[1], Ishaan Kapoor[1], Jake A. Swann[1], Caitlin A. Ashcroft[1], Simon N. Williams[1], Niall Conway[1], Amy Robinson[2], Clifford G. Kentros[2], Menno P. Witter[2], Simon J.B. Butt[1], and Adam M. Packer[1,✉]

[1]Department of Physiology, Anatomy, and Genetics, University of Oxford, Oxford, UK
[2]Kavli Institute for Systems Neuroscience, Centre for Neural Computation, Norwegian University of Science and Technology, Trondheim, Norway

The claustrum is highly interconnected with many structures in the brain, but the organizing principles governing its vast connectivity have yet to be fully explored. We investigated the defining characteristics and activity of single claustrum neurons, the nature of their relationship with the cortex, and their connectivity within the claustrum itself to gain a comprehensive view of claustral circuits. We show that the claustrum is composed of excitatory and inhibitory cell types that are connected through intraclaustral excitatory synapses, especially between neurons with disparate projection targets. Investigations of corticoclaustral innervation demonstrated that axons from the cortex localize to distinct dorsoventral modules depending on their region of origin. *In vitro* dual-color optogenetic mapping experiments revealed that individual claustrum neurons integrated inputs from more than one cortical region in a cell type- and projection target-specific manner. Integration in claustrum neurons was observed to be particularly common between areas of the frontal cortex and less so for sensory, motor, and association cortices. Finally, activity in claustrum axons in midline cortical areas recorded with *in vivo* two-photon calcium imaging showed responses to multimodal sensory stimuli. Our findings shed light on the organizing principles of claustrum circuits, demonstrating that individual claustrum neurons integrate cortical inputs and redistribute this information back to cortex after performing output target- and cell type-dependent local computations.

keywords: claustrum | connectivity | optogenetics | circuit-mapping | neuronal tract tracing | calcium imaging

Correspondence:
Adam Packer: adampacker@gmail.com,
Andrew Shelton: AndrewMcDowallShelton@gmail.com

Introduction

The claustrum (CLA) has been implicated in a variety of the sensory and cognitive functions of the brain including sleep (1, 2), salience detection (3, 4), multimodal integration (5–8), and task engagement (9, 10) (see also (11–13)). Furthermore, studies of lesions in the CLA note highly variable pathologies among patients that are consistent with a multifunctional role (14–16). Anatomical studies support this conclusion: the CLA is strongly and reciprocally connected with large swaths of the cortex in a projection pattern that has been previously described as a "crown of thorns" (17–20). CLA neurons connect particularly strongly to prefrontal and midline regions and appear to be segregated into connectivity-defined modules within the CLA (21, 22). Additionally, such connectivity-specific modules appear to have some functional selectivity (9, 23). Nonetheless, a comprehensive view of the circuit architecture underlying CLA function is not yet in sight in part because a full accounting of CLA connectivity and activity at the level of single neurons remains elusive.

Progress in identifying CLA cell types and circuit motifs *in vitro* has illuminated some aspects of how CLA neurons are wired and the implications this may have for their computations (21, 24, 25). Cortical projections to the CLA activate feed-forward inhibition via disynaptic connections with claustral interneurons and excitatory projection neurons, with the prevalence of both chemical and electrical synapses between interneurons supporting a dense local network of inhibition (25). Cortical afferents are targeted to CLA neurons based on the projection targets of claustral outputs, further underscoring the existence of a modular claustral network (21, 26–28). Recently, it has been discovered that cell types in the CLA are responsive to inputs from more than one cortical area, partly contradicting previous reports of unimodal sensory responses in different regions of the CLA of monkeys (29–31). However, these findings do not address which combinations of cortical inputs converge onto the CLA and onto which CLA neurons. Nor do they address whether any computations within the CLA occur, given the reach and strength of local inhibitory networks and the apparent sparsity of excitatory-excitatory connectivity (25). The question of whether the CLA acts as a cortical relay or a densely integrated crossroads of distributed cortical and subcortical networks remains unresolved.

One of the most striking aspects of the CLA is its widespread, reciprocal connectivity with the rest of the brain, but much remains to be uncovered about the rules governing this connectivity at the cellular level. Such a framework of CLA architecture represents a crucial foundation upon which we can develop a deeper understanding of the role of the CLA in brain function. It is from this perspective that we approached defining the cell types and circuitry of the CLA. By leveraging the input/output connectivity of the CLA, we sought to reveal the fine-scale organizing principles of CLA anatomy and physiology. Specifically, we aimed to determine (1) the anatomical boundaries of a projection-defined subset of CLA neurons, (2)

the intrinsic electrophysiological and morphological properties of these neurons (3) how intraclaustral, cortico-claustral, and claustrocortical connectivity mapped onto CLA cell types and modules, and (4) what modalities of sensory-related information CLA neurons might carry to cortex *in vivo*. This work provides mechanistic evidence of the CLA as an intrinsically integrative structure with the capacity to perform local transformations of cortical input via distinct intraclaustral pathways.

Results

Anatomical delineation of CLA in mice via retrograde tracing

To label CLA neurons in the adult mouse, we used a retrograde tracing strategy of injecting fluorescently labeled cholera toxin subunit B (CTB) into the retrosplenial cortex (RSP) (22, 32). To understand how CLA neurons differentially innervate RSP, we injected CTB488 (green), CTB555 (red), CTB647 (blue) into three separate rostrocaudal locations along the RSP (n = 3 mice, **Fig. 1a**). Confocal microscopy imaging of 100 μm-thick coronal sections revealed that each injection labeled highly overlapping populations of CLA neurons, distinct from the surrounding, unlabeled tissue (**Fig. 1b,c**, **Supp. Fig. S1**). A comparison between injection sites of labeling in CLA across mice revealed that the caudal injection site reliably labeled the most cells overall, especially in caudal regions of CLA (**Fig. 1d**, **Supp. Fig. S1**). Further, this strategy consistently demonstrated that retrosplenial-projecting CLA (CLA_{RSP}) neurons could be found along the whole CLA length, as defined by other sources (33–36). Moreover, the level of overlap between CLA neurons projecting to different regions of RSP varied depending on the injection site (**Fig. 1e**). We chose the caudal-most RSP injection site for the remainder of the study due to the dense and highly specific labeling of CLA_{RSP} neurons.

We next compared known markers of the CLA against the labeling of CLA_{RSP} neurons using immunohistochemistry to obtain a better understanding of the intraclaustral localization of CLA_{RSP} neurons (20, 34, 37–39) (n = 3 mice; **Fig. 1f**, **Supp. Fig. S2**). CLA_{RSP} neurons were aligned with the parvalbumin (PV) neuropil-rich CLA "core" and a paucity of myelinated axons in the same region, as shown by myelin basic protein (MBP). MBP also labeled densities of myelinated axons above and below the PV plexus, indicating dorsal and ventral aspects of the CLA. Therefore, CLA_{RSP} neurons were taken to represent a subpopulation of CLA neurons.

Analysis of thin (50 μm), sequential coronal sections revealed that the density of CLA_{RSP} neurons varied along the rostrocaudal axis (n = 3 mice; **Fig. 1g**) with the highest number of CLA_{RSP} neurons found around 1 mm rostral to bregma (1070 $\pm$ 261 cells/animal, 27 $\pm$ 11 cells/section; **Fig. 1h**). The rostral and caudal poles of CLA differed in that rostrally-located CLA_{RSP} neurons were found at low density, i.e. showing a dispersed distribution, whereas neurons found 1 mm caudal to bregma were densely packed in a relatively small cross-section of tissue. Together, these anatomical experiments enabled us to define and target a specific group of CLA_{RSP} neurons in subsequent electrophysiological investigations.

CLA neuron subpopulations based on intrinsic electrophysiology

To define CLA subpopulations with respect to their efferent projections, we repeated our retrograde labeling strategy to target both CLA_{RSP} neurons and non-CLA_{RSP} CLA neurons for acute *in vitro* whole-cell patch-clamp electrophysiology (**Fig. 2a,b**, see Methods). Recovered morphologies were matched with intrinsic electrophysiological profiles using a standardized, quality-controlled protocol for a final dataset of 540 neurons (**Fig. 2c**, **Supp. Fig. S3**). We identified several subtypes of both putative excitatory (total number of cells recovered: n = 434) and inhibitory (n = 106) neurons based on intrinsic electrophysiological properties (**Fig. 2d**).

Delineation of some subtypes was validated by unsupervised clustering on a dimensionally reduced dataset (**Supp. Fig. S3, Supp. Table 1**). While a significant proportion of putative excitatory neurons were CTB+, population-level homogeneity among this group impeded further clustering using unsupervised means. Rather, we relied on several intrinsic electrophysiological features – evident within the action potential waveform and firing pattern for each cell – to define four excitatory cell subtypes (E1-4). E1, E2, and E3 could be divided by spike amplitude adaptation normalized from the first action potential: E1 monophasically declined, E2 increased to a plateau, and E3 showed a biphasic pattern, initially declining sharply before recovering slightly (**Fig. 2e**). E4 neurons showed a similar pattern to E3 but more pronounced and also could be differentiated from all others by the presence of an afterdepolarization potential (ADP, 3.0 $\pm$ 2.2 mV; **Supp. Fig. S3**).

Interneurons, by contrast, could be easily categorized into four groups (high rheobase [HR], fast-spiking [FS], low threshold [LT], irregular [IR]), using unsupervised methods alone (average inhibitory silhouette score = 0.853, k = 4 clusters; **Supp. Fig. S3**). FS cells were found to fire narrow spikes between 50-200 Hz, while LT cells had a low rheobase and high input resistance. HR cells, conversely, had a large rheobase and low input resistance. Finally, IR cells fired irregularly and very infrequently compared to other types. Electrophysiological feature comparisons between these cells additionally supported distinct subtypes that differed from excitatory cells (**Fig. 2f**, **Supp. Fig. S3**; (40, 41)). Surprisingly, a small subset

of putative interneurons were found to be CTB+ (some of which were co-labeled with tdTomato in Nkx2.1-Cre;Ai9+ animal; **Supp. Fig. S4**), suggesting either the presence of further excitatory subtypes mixed within our interneuron cohort or the presence of inhibitory projection neurons within the CLA. These cells, the majority of which were HR neurons, represented 23% of our putative inhibitory subtypes and 5% of total CLA neurons (**Fig. 2d**, **Supp. Fig. S4**). While intrinsic electrophysiology easily disambiguated CLA interneuron subtypes, projection-defined approaches revealed novel interneuron characteristics not seen in electrophysiology alone.

We reconstructed 134 recovered morphologies (**Fig. 2d**) and found the majority of E1-4 subtype cells had spiny dendrites, consistent with them being excitatory neurons (**Supp. Fig. S5**). FS, HR, LT, and IR types were either aspiny or sparsely spiny in line with cortical GABAergic interneurons. This distinction aside, classical morphological analyses alone did not adequately define CLA cell types, again highlighting the need for connectivity- and function-defined approaches (**Supp. Fig. S5**, **Supp. Table 2**). Overall, our patch-clamp recorded neurons expand on previous knowledge of CLA neuron diversity, revealing a mix of excitatory and inhibitory neurons within the CLA_{RSP} region that vary in terms of their long-range connectivity to RSP.

Intraclaustral projections favor a cross-modular arrangement

Does excitatory-excitatory connectivity exist amongst neurons in the CLA_{RSP}-defined region? Different approaches to answering this question have previously provided different answers (32, 42, 43). To resolve whether such connectivity exists, we used a dual retrograde Cre (retroAAV-Cre) and CTB injection strategy in the RSP combined with conditional viral expression of AAV-FLEX-ChrimsonR-tdTomato in CLA (**Fig. 3a**). We then photostimulated presynaptic axon terminals throughout the rostrocaudal length of CLA while recording from either CTB+ or CTB- CLA neurons (**Fig. 3b**) and restricted analysis to monosynaptic connections with latencies of 3 - 12 ms, as reported by studies of opsin kinetics (44–46) (**Supp. Fig. S6**). We found that we could evoke short-latency, excitatory postsynaptic potentials (EPSPs) in the majority (69.5%; n = 32/46) of recorded CLA neurons, although only a small subset of these were CLA_{RSP} neurons (n = 4/11 CTB+ cells responsive; **Fig. 3c**). We additionally found that both excitatory and inhibitory neuronal subtypes exhibited EPSPs in response to CLA optogenetic stimulation (**Fig. 3d**, bottom right), although there were some differences between subtypes. Of the excitatory cell subtypes, E1 (72.7%) was more likely to receive local CLA_{RSP} input than E3 (53.8%) and E4 (66.6%) neurons, despite these latter two groups being the predominant subtypes in the CLA (**Fig. 3d**, top). Among inhibitory subtypes, FS neurons exhibited the highest probability of receiving CLA_{RSP} input (100%), while LT neurons received CLA_{RSP} input with probabilities (66.7%) comparable to that of excitatory types. Despite variability in these response probabilities, we found no statistically significant differences between cell types in the likelihood of responding to intraclaustral input ($p > 0.05$, Fisher Exact test between all types, Bonferroni corrected). These data suggest – with implications for information transfer within the CLA – that the primary factor underpinning the organization of intraclaustral connectivity is projection target, i.e. CLA neurons that project to areas outside of RSP are more likely to receive local input from those that do (CLA_{RSP}).

CLA neurons frequently form excitatory syanpses with each other but the anatomical relationship between pre- and post-synaptic CLA neurons remains unclear. However, during the course of this work, a novel transgenic mouse line, CC-EDGE::TRE-tight-THAG, became available that limited transgene expression to the CLA, dorsal endopiriform nucleus, and entorhinal cortex. We used this line to perform monosynaptic rabies-tracing to better understand the anatomical extent to which CLA neurons are connected across the rostrocaudal axis (**Fig. 3e**). This revealed that across animals (n = 13), 37.5% of all input neurons were located within the CLA compared to those located outside it ($p = 0.0013$; **Fig. 3f**). By using the rostrocaudal median position of starter populations as an anchoring point, we aligned intraclaustral input- and starter cells across animals to the same reference (**Fig. 3g**). As such, we could assess the rostrocaudal spread of intraclaustral monosynaptic inputs, relative to the starter populations. The vast majority of intraclaustral input cells were found within the same rostrocaudal sections as the starter cell populations, indicating that intraclaustral monosynaptic projections exist within local domains along the rostrocaudal axis. Notably, as shown by the tails of the centered input distribution, a few input cells were found further away from the starter cell populations, indicating the existence of longer-range intraclaustral projections (**Fig. 3g**).

Does stimulation of CLA neurons result in long-range excitation within the CLA? To answer this, we next turned to a horizontal slice preparation in rats using fluorescent voltage-sensitive dye (VSD RH-795; **Fig. 3h**, n = 13 rats, 28 recordings) to examine rostral-caudal connectivity *in vitro*. Electrical stimulation of the rostral pole of the CLA resulted in a traveling wave of increased voltage that spread to caudal CLA over a period of 10-15 ms (**Fig. 3i,j**). Blocking glutamate receptors by bath application of DNQX and APV abolished these responses, supporting a role for glutamatergic transmission within and along the rodent CLA (**Fig. 3j**, right, top and bottom). We additionally found that this transmission was bidirectional along the rostrocaudal axis – application of electrical stimulation in the caudal CLA elicited a wave of depolarization toward the rostral pole with similar temporal properties (**Supp. Fig. S6**). These experiments collectively point to an extensive

and bidirectional intraclaustral connectivity, engaging both excitatory and inhibitory neurons in a manner defined by efferent target. This further supports the idea that CLA contains the necessary circuitry to act as an integrative, excitatory hub for cross-modal associations.

Corticoclaustral inputs define a modular spatial organization

Multiple lines of evidence indicate that the CLA contains topographic zones of input and output in mice, yet it remains uncertain how these zones are organized spatially and physiologically. To resolve this, we again used a retrograde labeling method to distinguish CLA_{RSP}, now in tandem with the anterograde viral expression of tdTomato (AAV-ChrismonR-tdTomato) in one of several afferent neocortical areas: frontal (ORB, PL, ACAa, ACAp), motor (MOp), sensory (VISam, AUDd) and parahippocampal (ENTl) cortices (n = 3 mice/injection site, n = 24 mice in total; **Fig. 4a,b**, **Supp. Fig. S7**, see **Table 2** for full names of cortices). Coronal sections revealed variation in neocortical axon innervation relative to the CLA_{RSP} region along the dorsal-ventral axis. Several cortical areas, including ACAa and ORB, projected axons medially and laterally to CLA_{RSP} in addition to dorsally or ventrally, indicative of a core-shell structure (**Fig. 4c,d**, **Supp. Fig. S7**, and **S8**) akin to previously reported domains seen in output neurons of CLA ((22), **Fig. 4e,f**). The distinct dorsoventral patterns of innervation are best exemplified by the complementary projections from ORB, PL, and MOp, which target the ventral, core, and dorsal CLA, respectively (**Fig. 4e,f**).

We then investigated the physiological significance of this innervation by optogenetically stimulating presynaptic cortical axon terminals while recording from post-synaptic CLA neurons *in vitro* (**Fig. 4g,h**). We observed short-latency EPSPs in CLA neurons in response to optogenetic stimulation of axons arising from every neocortical injection site (n = 259 cells, 93 animals). However, there was variation in the percentage of responsive CLA neurons with stimulation of axons from frontal cortical areas – PL and ACAa having the highest probability of evoking a response in both CLA_{RSP} and non-CLA_{RSP} neurons. Stimulation of axons arising from sensorimotor areas such as AUDd and MOp had the lowest probability of evoking an EPSP with the notable exception of VISam. Further, CLA neurons were more likely to receive input from frontal cortical regions if they projected onward to RSP, i.e. were CTB+. This relationship was weaker or absent in other areas, such as MOp and AUDd, suggesting differences in the input-output routes of these CLA neurons. Results from these experiments confirm the modularity of CLA inputs and how those inputs map onto its outputs, but also raise questions regarding how the inputs may be combined onto single CLA neurons.

Dual-color optogenetic mapping reveals integration of cortical inputs

One of the posited functions of CLA is to affect sensorimotor "binding" or information integration (5, 15). Given the distinct topography of input axons (**Fig. 4**) and spatial organization of projection targets (22) of the CLA, we next set out to test if single CLA neurons in mice are responsive to more than one cortical region and, therefore, may support established models of CLA function. We combined retrograde tracer injections into the RSP with a dual-color optogenetic strategy, injecting AAV-Chronos-GFP and AAV-ChrimsonR-tdTomato into combinations of the neocortical regions (**Fig. 5a**) previously characterized (**Fig. 4**). Opsin-fluorophore expression was evident in axons localized in and around the region of CLA_{RSP} neurons during *in vitro* whole-cell patch-clamp recordings and *post hoc* histology (**Fig. 5b**).

Drawing from previously reported methodology (47, 48) of dual-color optogenetic stimulation, we used prolonged orange light (595 nm, 500 ms) to desensitize ChrimsonR opsins and reveal independent blue light-sensitive (470 nm, 4 ms) Chronos-expressing input (**Fig. 5c**, **Supp. Fig. S9**). Control experiments using one opsin confirmed the viability of this approach (n = 6 mice, 21 cells; **Supp. Fig. S9a-c**). We found that a subset of CLA neurons integrated cortical inputs (42/174 neurons with known CTB labeling, 66/259 of all tested cells; **Fig. 5d,g**). Similar to our single opsin observations, CLA_{RSP} neurons were more likely to integrate inputs from frontal areas than they were from other areas, although at least some neurons were found to integrate amongst all examined pairs (**Fig. 5d**). Integration was most common between ACAa and ORB (60%) and lowest between VISam and AUDd (17%). Less integration was observed when only one or neither of the input cortices were located in the frontal cortex. The measured probability of integration, however, was slightly higher than expected (ratio of measured:expected probability = 1.26 $\pm$ 0.12) based on the probability of receiving inputs from each cortical area individually, indicating that integration among single CLA neurons in these experiments occurred at a likelihood greater than response probabilities to individual cortical inputs would imply (**Fig. 5e**).

Concerning the electrophysiological identities of CLA neurons themselves, only E3, E4, and FS types received input from every cortical area (**Fig. 5f**, **Supp. Fig. S9**). Surprisingly, inputs from VISam (23%) and ENTl (43%) were more likely to target inhibitory cell types as a proportion of their inputs than most other cortical areas. IR cells were the only type found to receive input from only one area (ACA, n = 6 cells), though no IR neurons were recorded in experiments testing inputs from PL, MOp, AUDd, or VISam. Similarly, excitatory classes were differentially innervated by the cortex. For example, 50% of all VISam inputs were to E3 neurons, while only 20% of MOp were onto E3 neu-

rons. By contrast, 50% of MOp inputs were devoted to E4 neurons while 23% of VISam inputs were to E4 neurons.

Integration of cortical inputs was more prevalent in certain cell types as well (**Fig. 5g**). 30% of E3 and E4 neurons and 48% of all recorded FS interneurons were found to integrate cortical input, irrespective of the combination of cortical input, congruent with their response probabilities to individual cortices (**Fig. 5f**, **Supp. Fig. S9**). A large proportion (21%) of LT neurons were also found to integrate despite making up less than 10% of all neurons recorded. E1, E2, HR, and IR types showed little to no propensity for integrating any cortical inputs. We find that E3 and E4 neurons and FS interneurons are the most likely to integrate information from the cortex, while other excitatory and inhibitory cell types may participate in different circuits or have a dedicated and unitary region of input. These findings support the idea that CLA is a functionally diverse structure with integrative and modality-specific components.

Claustrocortical outputs provide multimodal information differentially across layers in downstream cortical regions

To explore how CLA influences the neocortex, we returned to our retro-Cre conditional expression of opsin in CLA_{RSP} neurons (**Fig. 6a**), focusing on outputs to ACA and RSP (**Fig. 6b,c**). Cells in ACA or RSP were filled with biocytin during recording for *post hoc* analysis of their location within the cortical laminae (**Fig. 6c**). Axonal fluorescence from CLA neurons varied by cortical layer in these regions (**Fig. 6d**). Optogenetic stimulation of CLA axons evoked both inhibitory postsynaptic currents (IPSCs) and excitatory postsynaptic currents (EPSCs) in cortical neurons during voltage-clamp at holding potentials of 0 mV and -70 mV, respectively (**Fig. 6e**). Similarly to other experiments, we restricted analysis of EPSCs to monosynaptic connections with latencies of 3 - 12 ms (44) (**Fig. 6f,g**, **Supp. Fig. S10**). The longer latency to onset of IPSCs (7 - 15 ms) suggests recruitment of feed-forward inhibition by CLA neurons in both cortical areas, though some short latency IPSCs could be due to direct long-range inhibitory projections (**Fig. 2d, Supp. Fig. S10**). PSCs could be evoked relatively evenly across most cortical layers of ACA (n = 49 cells; **Fig. 6h**, top). In RSP, we observed the highest response probability in L5, but responses in deep layers overall were reduced compared to ACA (n = 43 cells, **Fig. 6h**, bottom). Finally, we found that superficial (L2/3) and deep (L5 & L6) layer excitation and inhibition were both statistically different between ACA and RSP (EPSC $p = 0.0003$, IPSC $p = 0.026$, Cochran–Mantel–Haenszel test). These experiments point to a complex interaction with target cortical areas that are both cortex and layer-dependent.

We next sought to understand what signals CLA conveys to the cortex *in vivo*. We injected mice with a retro-Cre virus in ACAa and RSP and a Cre-dependent calcium indicator (AAV-FLEX-GCaMP7b) in the CLA. Mice were subsequently implanted with cranial windows centered above bregma for observation during two-photon calcium imaging (78 recordings from 4 animals including 1364 axon segments; **Fig. 7a**, left). Congruent with previous experiments, the expression of GCaMP7b was restricted to CLA neurons, and axons from these neurons were visible in the cortex (**Fig. 7b**, **Supp. Fig. S11**). GCaMP7b labeled axons were recorded throughout the cranial window.

During recording, mice were exposed to stimuli intended to evoke responses in different sensory modalities: a flash of light, stimulation of the whisker pad via a piezo-controlled paddle, and/or a complex auditory tone (**Fig. 7a**, right). Stimuli were randomized at 8-11 second intervals and interleaved with a "blank" period in which no stimulus was delivered (**Fig. 7c**). 47% of tested axons displayed significant calcium transients to at least one stimulus modality during passive presentation and all modalities could evoke responses in at least some CLA axons (**Fig. 7d,e**). Interestingly, 35% of stimulus-responsive CLA axons were exclusively responsive to multimodal trial types, while 15% were exclusively responsive to unimodal trial types (**Fig. 7f**). Somatosensory stimuli (whisker) were the most likely to elicit changes in fluorescence, followed by light and then sound. The proportion of responsive axons tended to be highest when stimuli were combined (**Fig. 7g**). Experiments were repeated using only unimodal stimuli (i.e. sound, light, and whisker only) and similar results were obtained (117 recordings from 4 animals including 1342 axon segments; **Supp. Fig. S12**). These results are consistent with our *in vitro* recordings that suggested input integration among CLA neurons was a common occurrence and/or that CLA neurons receive input from one cortex that contains neurons of mixed-selectivity (**Fig. 5**). In short, the CLA integrates at both the anatomical and functional levels.

These data collectively build on previous work aimed at understanding CLA activity in the cortex. CLA axons can carry signals derived from unimodal or multimodal sensory inputs and differentially innervate downstream targets depending on the cortical layer and cortical area in question. Moreover, based on axonal morphology shown in other works (20) and input mapping demonstrated here, single CLA_{RSP} neurons appear to be capable of integrating diverse input information and then redistributing the transformed signal across the cortex.

Discussion

By exploiting CLA projections to RSP using a retrograde labeling approach, we identified several electrophysiological CLA cell types and assessed their role in corticoclaus-

tral, intraclaustral, and claustrocortical circuits. Our results show that individual CLA neurons integrate diverse information from across the cortex, participate in specific intraclaustral networks, and are capable of broadcasting sensory-related information to the cortex in a region- and layer-specific manner.

A key difficulty in researching CLA neurons is defining the CLA itself. Decades of neuronal tract-tracing and immunohistochemical studies have provided crucial information about the expression patterns and connectivity profiles of CLA neurons (recently reviewed in (12)). More recent work using transgenic or viral strategies have enabled labeling the CLA in different ways (also reviewed in (12)); see also (20, 49–51)). However, caveats that are inherent in these methodologies yield varyingly non-specific access to CLA neurons. In this work, we used a retrograde tracing strategy in the RSP to label a specific set of CLA neurons as motivated by recent studies (22, 32, 52). The RSP is uniquely positioned for use in this technique as it does not receive inputs from structures around the CLA but receives specifically dense innervation from the CLA itself. We found that CLA_{RSP} neurons span the rostrocaudal axis of the CLA and align with previously identified markers of the CLA "core" (34, 38, 39, 53). Retrograde tracing from RSP offered a simple method for accurately assessing the anatomical and physiological features CLA neurons in later experiments.

Disparate accounts have been reported of CLA neurons' intrinsic electrophysiological properties, which poses a challenge when trying to determine the role of CLA neuronal subtypes in brain activity (24, 25, 54, 55). From our perspective, this disparity could arise from uncertainty over which group of CLA neurons is being recorded between studies. Retrograde labeling of CLA_{RSP} proved useful for targeted investigations of CLA electrophysiology *in vitro* using a standardized protocol (56, 57). From our recordings across a large population of both CLA_{RSP} and non-CLA_{RSP} neurons, it was evident that a heterogeneous mix of spiny, excitatory neurons and aspiny, inhibitory neurons exist in the CLA, consistent with other studies (24, 53, 58). These broad categories could be further subdivided into smaller subgroups consisting of four electrophysiological types in each. Similar to the cortex (59), excitatory neurons were found to be relatively homogeneous from an unsupervised clustering perspective but could nevertheless be differentiated by their AP waveforms and variability in their tendency to project to RSP. Though direct comparisons are difficult, the E1, E3, and E4 subtypes closely matched excitatory cell types found in recent investigations of CLA intrinsic electrophysiology (24).

Low within-group and high between-group variability among inhibitory neurons accurately distinguished subtypes using unsupervised methods. Many of these inhibitory interneuron subtypes are similar to those observed in the neocortex (60). In addition, we found multiple lines of evidence indicating the existence of a substantial subpopulation of inhibitory projection neurons, which have also been observed in prefrontal cortex, amygdala, hippocampal areas, entorhinal cortex, and the subplate (45, 61–66). This not only highlights its similarity to other forebrain structures (67) but also suggests previously unconsidered functional possibilities for the CLA. These putative monosynaptic inhibitory inputs may provide another route by which CLA exerts a direct suppressive influence on the cortex (see also below).

Hypotheses that position the CLA as affecting cross-modal processing (68, 69), synchronization (6, 7), or integration (5, 8) implicitly rely on a substantive intraclaustral excitatory network to link projection neurons across its considerable length. Conflicting evidence thus far has not been able to deliver a satisfying answer to whether such connectivity exists and, if so, with what specificity (25, 32, 42, 43, 54). Here, we used a dual-retrograde and conditional opsin expression strategy to understand if such connections are present in the CLA. We found that excitatory connections are quite common in the CLA and broadly target most CLA excitatory and inhibitory types. Additionally, we observed that this connectivity was less biased toward inhibitory types than previously thought (25), but was influenced more by the output target of postsynaptic CLA neurons. Anatomical rabies tracing and VSDI experiments further suggested that the major axis along which excitatory connectivity acts is rostrocaudal. Data obtained here offer critical insights into the types of computations the CLA is capable of performing, underpinning the existence of a neural substrate for local processing.

Much like CLA efferents (22), we found that cortical projections to CLA arrange into modules along the dorsoventral axis. Interestingly, certain cortices such as ORB and ACAa "cupped" CLA_{RSP} both medially and laterally in addition to dorsally or ventrally. Physiological investigations of cortical input revealed that CLA_{RSP} neurons are more likely to respond to frontal cortical regions than non-CLA_{RSP} neurons. CLA_{RSP} neurons were also more likely than non-CLA_{RSP} neurons to respond to motor and association cortices. Surprisingly, however, we found that CLA neurons, especially non-CLA_{RSP} neurons, were far more likely to respond to secondary visual cortex input *in vitro*, more so than has been reported in primary sensory cortices (21, 70). These findings both confirm the deep ties between CLA and frontal areas associated with top-down cognitive functions and suggest higher responsiveness to more highly processed sensory information.

The patterning of cortical axons in the CLA of mice is simultaneously segmented, with identifiable dorsal, core, and ventral modules, while also forming an overlapping gradient (18) that blends input streams to CLA neurons. From an anatomical perspective, we thought it very likely that CLA neurons in mice instantiate multimodal integration at the level of single cells given the overlap of cortical afferents within it, despite previous reports of unisensory modules in the CLA of cats and monkeys (31, 71, 72).

To test whether this was the case, we used a dual-color optogenetic input mapping strategy to assess the responsiveness of CLA_{RSP} neurons and non-CLA_{RSP} neurons to more than one cortical area *in vitro* (29). Our findings demonstrate that individual CLA neurons are frequently responsive to multiple different inputs. This was especially true for CLA_{RSP} when the cortices in question were both frontal, while the balance of responsiveness shifted to non-CLA_{RSP} when other cortical areas were involved. Overall, cell type identity, as defined by intrinsic electrophysiology and efferent projection target, influenced the likelihood that a neuron was dual-responsive to afferent input in the CLA.

Our final set of experiments sought to investigate the regional and laminar differences of CLA innervation of the cortex as well as the types of sensory-related information CLA axons convey to their cortical targets. Recent *in vivo* electrophysiological evidence points toward differences in excitatory and inhibitory tone elicited by excitation of CLA cell bodies that varies by cortical area and layer (9, 51). Other studies in single cortical regions find more uniform responses to CLA inputs, generally inhibitory (73, 74), although electrophysiological studies in cats have found more variable or bidirectional responses in visual cortices (75, 76). We chose to investigate CLA_{RSP} connections to ACA and RSP *in vitro* and *in vivo* – ACA for the dense connectivity it shares with CLA (and CLA_{RSP}) and RSP for the known properties of neurons that project there. From *in vitro* studies, we found that CLA axons innervate the cortical layers of ACA and RSP differently. Overall, ACA was innervated in deep layers more than RSP for excitation and inhibition. These results demonstrate the CLA exhibits a variable influence over cortical function that is both region- and layer-dependent.

Our *in vivo* calcium imaging experiments concurrently confirmed that axons of CLA_{RSP} neurons can carry representations of sensory stimuli to cortical regions. Moreover, we found CLA axons were frequently responsive during stimulation, implying the CLA actively participates during the processing of sensory information. This finding contrasts with recent studies in mice (49, 50) in which CLA neurons were infrequently responsive to sensory stimulation *in vivo*. The disparity between these results may be explained by methodological differences. Both studies used different methods of labelling CLA neurons: Ollerenshaw et al used a transgenic line (Gnb4) while Chevée et al optotagged neurons based on their projections to somatosensory cortex. While the Chevée et al study used a similar retrograde labelling strategy, they likely still targeted a different subpopulation of CLA neurons (22). Additionally, both studies also used different techniques to record neural activity. Ollerenshaw et al used calcium imaging to record responses in CLA neurons directly, requiring the implantation of a GRIN lens, which may reduce the transmission of inputs to the CLA. Chevée et al used less invasive extracellular electrophysiological recordings, but this required *post-hoc* confirmation of CLA identity that cannot precisely map each recorded neuron back onto its exact location in the tissue. Finally, we observe the strongest responses to whisker stimulation with a paddle in mice with all whiskers intact, which neither Ollerenshaw et al nor Chevée et al incorporated into their studies (Chevée et al used single whisker stimulation).

Common among hypotheses of CLA function is the importance of its deep ties to higher-order circuits that imply a role in higher-order processes. Our work showing that claustrum integrates inputs at the structural and functional levels may indicate a role in coincidence detection, as has been stated in other studies (21, 25). CLA neurons may, for example, spike more often when conjunctive stimuli appear in two different sensory streams (e.g. a loud sound accompanied by a bright flash), providing an all-or-none signal. Another role could be in yoking together different streams of input based on their temporal synchrony (77). CLA neurons may be more active when a given amount of synchronicity in its inputs arises, making its signals informative in a graded as opposed to all-or-none fashion. The internal, cross-modular, and recurrent excitation within the CLA could also allow for a degree of temporal synchronization between its input cortices through reverberant cortico-claustral loops (6, 8). Finally, the integrative properties of the CLA could provide the substrate for transforming the information content of its inputs. This could be useful for facilitating responses to weak but conjunctive stimuli, reducing the trial-to-trial variability of responses to conjunctive stimuli, and/or increasing the signal-to-noise of neural activity in response to conjunctive stimuli (78). The results of such computations could enable the CLA to modulate cortical activity through the direct or disynaptic inhibition of cortical circuits, either to amplify behaviorally-relevant processes, diminish irrelevant activity, or both (73). In these ways, the CLA could be a regulator of global interactions across the cortex in a modular manner tailored to each cortical target.

In summary, we find that the CLA, specifically CLA_{RSP}, participates in a complex circuit with both the cortex and other CLA neurons that is specified by intrinsic electrophysiological type and efferent projection target. CLA neurons are broadly capable of synthesizing a wide range of cortical inputs at the level of single neurons, a finding that supports the idea of CLA acting as a cortical network hub. The presence of a robust internal network of excitatory CLA neurons additionally supports the view that the CLA performs local computations. These computations then differentially influence downstream cortical processing in a regional- and layer-specific manner that may depend on the specific CLA output modules that are active at the time. The fast monosynaptic connections investigated in this study could give rise to cortical synchronization or oscillations through these integrative and cross-modular CLA networks. The fundamentally integrative nature of the claustrum at the anatomical and functional levels suggests

it is involved in the highest levels of behavior, possessing the crucial neural substrates for a diverse and powerful effect on higher-order brain function.

Materials & Methods

Animal usage

Animal procedures were subject to local ethical approval and adhered to the United Kingdom Home Office (Scientific Procedures) Act of 1986. Male and female C57BL/6J or Nkx2.1Cre;Ai9 mice were used in these experiments. Mice were between 3-11 weeks of age when surgery was performed. CC-EDGE::TRE-tight-THAG transgenic mice and Long-Evans rats were used in experiments conducted at the Kavli Institute for Systems Neuroscience at the Norwegian University of Science and Technology (NTNU), Trondheim. These experiments were approved by the Federation of European Laboratory Animal Science Association (FELASA) and local authorities at NTNU. CC-EDGE transgenic mice were provided by Dr. Stefan Blankvoort (79, 80), while TRE-tight-THAG transgenic mice were provided by Dr. Rajeevkumar R. Nair.

Surgical Procedures

Cortical and claustral injections of viruses and/or retrograde tracers were performed in mice aged p22–40. Briefly, mice were anesthetized under 5% isoflurane and placed in a stereotaxic frame before intraperitoneal injection of 5 mg/kg meloxicam and 0.1 mg/kg buprenorphine. Animals were then maintained on 1.5% isoflurane and warmed on a heating pad at 37℃ for the duration of the procedure. The scalp was sterilized with chlorhexidine gluconate and isopropyl alcohol (ChloraPrep). Local anesthetic (bupivacaine) was applied under the scalp two minutes prior to making the initial incision. The scalp was then incised along the midline and retracted in order to expose the skull, which was then manually leveled between bregma and lambda. Target regions were found using coordinates derived from the Paxinos & Franklin Mouse Brain Atlas (3rd ed.) (33) and marked onto the skull manually (see Table 1 for coordinates). Craniotomies were performed using a dental drill (500 μm tip) at 1-3 sites above the cortex. Craniotomies were made exclusively in the right hemisphere unless otherwise noted. Pulled injection pipettes were beveled and back-filled with mineral oil before being loaded with one or more of the following: AAV1-Syn-ChrimsonR-tdTomato (Chrimson, 2.10e+13 gc/mL, 250 nL, Addgene #59171-AAV1), AAV5-Syn-FLEX-rc[ChrimsonR-tdTomato] (FLEX-Chrimson, 1.20e+13 gc/mL, 250 nL, Addgene #62723-AAV5), AAVrg-hSyn-Cre-WPRE-hGH (retro-Cre, 2.10e+13 gc/mL, 80 nL, Addgene #105553-AAVrg) (81), AAV1-Syn-Chronos-GFP (Chronos, 2.90e+13 gc/mL, 250 nL, Addgene #59170-AAV1), AAV-syn-FLEX-jGCaMP7b-WPRE (FLEX-GCaMP7b, 1.90e+13 gc/ml, 250nl, Addgene #104493-AAV1), Cholera Toxin Subunit B (Recombinant) Alexa Fluor™ 488/555/647 Conjugate (CTB-488/555/647, 0.1% wt/vol, 80 nL, ThermoFisher C34775/C34776/C34778). Pipettes were lowered to the surface of the pia at the center of the craniotomy and zeroed before being lowered into the brain. The pipette was allowed to rest two minutes prior to injection of substances, at which point injection took place at 5-10 μl/sec. Pipettes were allowed to rest for ten minutes after injection. The incision was sutured with Vicryl sutures and sealed with Vetbond (3M) after all craniotomies and injections had been made. Mice were then transferred to a fresh cage and allowed to recover. Mice were supplied with edible meloxicam jelly during post-op recovery for additional analgesia.

Table 1. Stereotaxic injection coordinates. DV coordinates measured as depth from pia.

Target Area	AP (mm)	ML (mm)	DV (mm)
CLA	1.0	3.4	-2.7
RSPr	-1.75	0.50	-1.00
RSPi	-2.25	0.50	-1.00
RSPc	-3.00	0.50	1.00
ACAa	1.34	0.30	-1.25
ACAp	0.11	0.25	0.90
PL	1.50	0.60	-1.80
ORB	2.50	1.20	-1.80
MOp	0.60	1.50	-0.75
ENTl	-4.30	3.50	2.25
VISam	-2.70	1.50	-0.50
AUDd	-2.12	3.75	-0.50

Mice to be implanted with cranial windows first received intracranial injections as described above. Once fully recovered from the injection surgery, mice were re-anesthetized for window implantation. Surgical preparation, anesthesia, analgesia, and recovery procedures were the same as for intracranial injection surgeries. Following sterilization of the scalp, a section was removed. The skull was then cleaned to remove the periosteum. An aluminum headplate with an imaging-well centered on bregma was then secured in place with dental cement (Super-Bond C&B, Sun-Medical). A 4 mm circular craniotomy centered on bregma was then drilled. After soaking in saline, the skull within the craniotomy was removed. The craniectomy was then flushed with sterile saline to clean any bleeding. A durotomy was then performed over the right hemisphere. A cranial window composed of a 4 mm circular coverslip

glued to a 5 mm circular coverslip was pressed into the craniotomy and sealed with cyanoacrylate (VetBond) and dental cement. Mice were then allowed to recover fully before any further experimental procedures.

Surgical procedures for rabies tracing injections on CC-EDGE::TRE-tight-THAG mice followed the same steps as described above, with the following exceptions. Analgesics were given as subcutaneous injections of 1mg/kg Metacam and 0.1mg/kg Temgesic, and 1mg/kg Marcaine was injected subcutaneously as a local anesthetic. Animals were between 11 and 23 weeks old and the tissue was collected 10-14 days post-surgery.

In vitro slice preparation

Acute coronal brain slices (300 μm thick) were prepared from tracer- and/or virus-injected mice (average age at time of experimentation = p52). Slices from virus-injected mice were prepared exclusively 3-5 weeks post-injection. Mice were deeply anesthetized with 5% isoflurane and transcardially perfused with ice cold NMDG ACSF of the following composition: 92 mM N-Methyl-D-Glucamine (NMDG), 2.5 mM KCl, 1.25 mM NaH_2PO_4, 30 mM $NaHCO_3$, 20 mM HEPES, 25 mM glucose, 2 mM thiourea, 5 mM Na-ascorbate, 3 mM Na-pyruvate, 0.5 mM $CaCl_2{\cdot}4H_2O$ and 10 mM $MgSO_4{\cdot}7H_2O$, 12 mM N-acetylcysteine (NAC), titrated pH to 7.3–7.4 with concentrated hydrochloric acid, 300-310 mOsm. The brain was then extracted, mounted, and sliced in ice cold NMDG ACSF on a Leica VT1200s vibratome or a Vibratome 3000 vibratome. Slices were incubated in NMDG solution at 34℃ for 12-15 minutes before being transferred to room temperature HEPES holding ACSF of the following composition for 45-60 minutes before experimentation began: 92 mM NaCl, 2.5 mM KCl, 1.25 mM NaH_2PO_4, 30 mM $NaHCO_3$, 20 mM HEPES, 25 mM glucose, 2 mM thiourea, 5 mM Na-ascorbate, 3 mM Na-pyruvate, 2 mM $CaCl_2{\cdot}4H_2O$ and 2 mM $MgSO_4{\cdot}7H_2O$, 12 mM NAC, titrated pH to 7.3–7.4 with concentrated hydrochloric acid, 300-310 mOsm. All solutions were continuously perfused with 5% CO_2/95% O_2 from 20 minutes prior to use.

For *in vitro* VSDI experiments, slices (400μm thickness) were prepared from n=13 Long–Evans rats (100–150 g). Before the procedure, the rats were anesthetized with isoflurane (Isofane, Vericore), before being decapitated. Brains were extracted from the skull and placed into an oxygenated (95% O_2–5% CO_2) ice-cold solution of ACSF, made with the following (mM): 124 NaCl, 5 KCl, 1.25 NaH_2PO4, 2 $MgSO_4$, 2 $CaCl_2$, 10 glucose, 22 $NaHCO_3$. The brains were sectioned at an oblique horizontal place (front tilted 5 degrees downwards).

Slices were then moved to a fine-mesh membrane filter (Omni pore membrane filter, JHWP01300, Millipore) held in place by a thin Plexiglas ring (11 mm inner diameter; 15 mm outer diameter; 1–2 mm thickness) and kept in a moist interface chamber, containing previously used ACSF and continuously supplied with a mixture of 95%O_2 and 5% CO_2 gas. Additionally, the slices were kept moist from gas being led through ACSF before entering the chamber. The ACSF was kept at 32℃. Slices were allowed to rest for at least 1h before use, one by one in the recording chamber superfused with ACSF.

Cell identification & electrophysiological recording

Individual slices were transferred to a submersion chamber continuously superfused with bath ACSF of the following composition: 119 mM NaCl, 2.5 mM KCl, 1.25 mM NaH_2PO_4, 24 mM $NaHCO_3$, 12.5 mM glucose, 2 mM $CaCl_2{\cdot}4H_2O$ and 2 mM $MgSO_4{\cdot}7H_2O$, titrated pH to 7.3–7.4 with concentrated hydrochloric acid, 300-310 mOsm, held at 32℃, and perfused with 5% CO_2/95% O_2 for 20 minutes prior to use. Neurons were visualized with a digital camera (Hammamatsu ORCA-Flash4.0 V3 C13440) and imaged under an upright microscope (Sutter Instruments) using 10X (0.3 NA, Olympus) and 40X (0.8 NA, Zeiss) objective lenses and transmitted infrared light or epifluorescence in various wavelengths.

CLA neurons were identified in acute slices by one of several methods. First, in the majority of experiments, neurons were patched within the subregion of retrogradely labeled somas following CTB injection in the RSP. Additionally, in most experiments we also used fluorescently-labeled corticoclaustral axons from two different sources to further identify the CLA. In a small subset of experiments in Nkx2.1-Cre;Ai9 animals, we were also able to visualize a tdTomato-labeled dense plexus of fibers in the CLA that matches with previous identifications of the CLA relying on a dense plexus of parvalbumin-positive fibers(22, 25, 37, 39).

Borosilicate glass pipettes (4-8 MΩ, 1-3 μm tip outer diameter) were pulled using a Narishige PC-10 two-step puller with steps at 65.1℃ and 44.2℃ and filled with an intracellular solution for electrophysiological recordings of one of the following compositions: 1) 128 mM K-Gluconate, 10 mM HEPES, 4 mM NaCl, 5 mM Mg-ATP, 0.3 mM Li_2-GTP, 2 mM $CaCl_2$, 8.054 mM biocytin, pH 7.2, 285–290 mOsm. 2) 110 mM Gluconic acid, 40 mM HEPES, 5 mM $MgCl_2$, 0.2 mM EGTA, 2 mM ATP, 0.3 mM GTP, 5 mM lidocaine, 8.054 mM biocytin, pH 7.2 with CsOH, 285–290 mOsm.

Whole-cell patch-clamp recordings were made from single neurons using a Multi-Clamp 700B amplifier (Molecular Devices) in current-clamp mode and controlled with custom protocols in PackIO (82). Briefly, neurons were approached in voltage-clamp (0 mV) with intracellular solution back-filled pipettes under positive pipette pressure and 40X magnification. Negative pressure was applied once a small dimple in the membrane could be seen and was

held (-60 mV) until >1 GΩ seal had formed, after which the seal was broken and recording began. Recordings were low-pass filtered at 10 kHz and digitized at 10 or 20 kHz. Results were not corrected for the -14 mV liquid junction potential during current-clamp experiments and the -0.69 mV junction potential in voltage-clamp experiments. The chloride reversal potential in each case was -72 mV and -65 mV, respectively.

To be included for further analysis, patched neurons needed to pass a number of quality-control criteria during recording of intrinsic profiles. These included R_{access}< 35 MΩ or < 20% of R_{input}, relative action potential amplitude at rheobase > 50 mV and an absolute amplitude above 0 mV, I_{hold} > -30 pA, absolute drift from baseline (measured from the beginning of the recording) < 10 mV, and a resting membrane potential < -50 mV.

In most cases, only one CLA neuron was patched per slice to prevent ambiguity during morphological reconstruction. Once recordings were complete, neurons were allowed to fill with biocytin for up to 30 minutes, after which the pipette was withdrawn from the tissue and slices were transferred to 4% paraformaldehyde (PFA).

Optical system for *in vitro* visualization / photostimulation

The optical system used for *in vitro* visualization and photostimulation combined blue (Thorlabs M470L4), orange (Thorlabs M595L3), and far-red (Thorlabs M625L3) LED paths. Briefly, orange and far-red LED paths were combined via a 50/50 beamsplitter (Thorlabs BSW10R), then passed through a blue/red combining dichroic mirror (Thorlabs DMLP505R). Light was then passed down onto the sample through either a RGB dichroic mirror (Laser2000 FF409/493/573/652-Di02-25x36) for epifluorescence visualization or a "cold" mirror (Thorlabs FM03R) for photostimulation. Tissue was visualized via 850 nm light transmitted through a condenser mounted beneath the slice chamber (Thorlabs M850L3). Incident and reflected light passed through excitation (Semrock FF01-378/474/554/635-25) and emission (Semrock FF01-432/515/595/730-25) filters while in RGB visualization mode.

In vitro photostimulation of AAV-ChrimsonR-tdTomato & AAV-Chronos-GFP

In experiments where opsin-expressing viruses were injected into either the cortex or CLA, a number of different optogenetic photostimulation protocols were used. Briefly, 470/595 nm LEDs were used to deliver light pulses (4 ms or 500 ms) through a 40X objective lens. LED power on the sample was titrated to the minimum power required to elicit a response in each cell. 470 nm LED power under the objective lens ranged between 0.069 mW and 3.99 mW and was typically 0.6 mW. 595 nm LED power under the objective lens ranged between 0.61 mW and 4.4 mW and was typically 1.22 mW. With the exception of dual-color sequential stimulation, all light pulses were separated by 10s to allow sufficient time for opsins to resensitize.

For dual-color sequential photostimulation, contributions of each cortical presynaptic input axon expressing either Chrimson or Chronos were assessed separately by photostimulation with 470 or 595 nm light pulses (4 ms). To disambiguate 470 nm-evoked Chrimson responses from 470 nm-evoked Chronos responses, 595 nm light was pulsed for 500 ms followed immediately by a brief 4 ms 470 nm pulse in order to desensitize Chrimson opsins expressed in presynaptic terminals before Chronos stimulation. All photostimulation experiments were repeated ten times and averaged.

For experiments in which FLEX-Chrimson was expressed directly in CLA neurons via retro-Cre injection into RSP, non-expressing CLA neurons were patched and stimulated using 595 nm light (4ms) at both 0.1 Hz. 595 nm light was typically set at 1.22 mW power on sample. The same protocol was used during voltage-clamp recording of cortical neurons in response to CLA axon stimulation.

Morphological recovery

Patched tissue was fixed in 4% PFA for 2 hours or overnight as described above. Sections were then removed from PFA and washed 3 x 5 minutes in 0.01M PBS. Sections were then transferred to 0.25% PBST and allowed to incubate in streptavidin for at least three days (1:500 Streptavidin, Alexa Fluor™ 488/647 conjugate, ThermoFisher S11223/S21374). Tissue was then washed 3 x 5 minutes in 0.01M PBS, mounted, coverslipped, and imaged as described below.

Perfusion & tissue sectioning

Mice were deeply anesthetized with 5% isoflurane before receiving an overdose of pentobarbital via intraperitoneal injection. Mice were then transcardially perfused with 0.01M phosphate buffered saline (PBS), followed by 4% paraformaldehyde (PFA). The brain was then extracted and allowed to fix in 4% PFA overnight. Brains were then moved to 0.01M PBS and mounted for sectioning on a Leica VT1000s vibratome. Slices were sectioned coronally to 50 μm or 100 μm thickness and placed in 0.01M PBS before immunohistochemistry and mounting or stored in tissue freezing solution (TFS, 45% 0.01M PBS, 30% ethylene glycol, 25% glycerol) at -20℃ for up to three years.

Immunohistochemistry & imaging

Mice were perfused and sections were collected as above. Sections were first washed 3 x 5 minutes 0.01M PBS before permeabilization in 0.01M PBS and 0.5% TritonX (PBST) for 2 x 10 minutes. Sections were then blocked for 90 minutes in PBST and 5% normal goat or donkey serum at room temperature, after which they were incubated in primary antibody (mouse anti-MBP 1:500, Merck NE1019, RRID:AB_604550; rabbit anti-PV 1:400–500, Swant PV27a, RRID:AB_2631173; chicken anti-GFP 1:2500, AVES GFP-1020, RRID: AB_10000240) for at least 48 hours at 4℃. The slices were then washed 3 x 5 min in 0.5% PBST followed by incubation in secondary antibodies (goat anti-mouse Alexa Fluor 405 1:500, Invitrogen A31553, RRID:AB_221604; goat anti-rabbit Alexa Fluor 488 1:500, Invitrogen A11034, RRID:AB_2576217; donkey anti-rabbit Alexa Fluor 594 1:500, Jackson ImmunoResearch 711-585-152, RRID:AB_2340621; Donkey anti-chicken Alexa Fluor 488 1:500, Jackson ImmunoResearch 703-545-155, RRID:AB_2340375) for 3 hours. Finally, tissue was washed in 0.01M PBS for 3 x 5 minutes, then mounted and coverslipped.

Once dry, whole slice and CLA images were taken at 4X and 10X magnification (UPlanSApo, 0.16 and 0.4 NA) on an Olympus FV3000 laser scanning confocal microscope. For recovered morphologies, images were taken on the above microscope or on a Zeiss LSM710 confocal laser scanning microscope at 20X magnification and tiled across the z-axis, or on a custom 2p microscope at 16X magnification (Coherent Vision-S laser, Bruker 2PPlus microscope, Nikon 16X 0.8 NA objective). Images of post-hoc histology from calcium imaging animals were taken on a Ziess LSM710 at 10X magnification tiled across the z-axis, or a Leica epifluorescence microscope (1.6X). Slices and morphologies were not corrected for tissue shrinkage as a result of fixation.

Intraclaustral connectivity mapping based on rabies tracing data

A detailed description of rabies tracing procedures and methods can be found in (34). Briefly, EnvA-pseudotyped, G-protein deleted CVS-N2c recombinant rabies virus expressing tdTomato (RABV-tdTomato) was used in these experiments. The virus was provided by Dr. Rajeevkumar R. Nair and produced at the Viral Vector Core at the Kavli Institute for Systems Neuroscience. CC-EDGE::TRE-tight-THAG transgenic mice express TVA receptors and rabies glycoprotein in a subset of cells largely confined to the CLA complex. Primary infection is thus restricted to these cells. Primary infected cells (starter cells) were classified by immunohistochemically staining against the 2A linked protein found in TVA expressing cells and an RFP tag expressed by the rabies virus, visualized by immunohistochemical labeling. Intraclaustral inputs were identified by the expression of the RFP tag but not the 2A-linker protein, as these cells lack the TVA receptor.

Voltage-sensitive dye imaging

Slices were stained for 3 minutes with VSD RH-795 (R649, Invitrogen, 0.5% in ACSF) and imaged in a recording chamber positioned beneath a fluorescence microscope (Axio Examiner, Zeiss). The slices were excited with 535 ± 25 nm light (bandpass), reflected by a dichroic mirror (half reflectance wavelength of 580 nm) and epifluorescence was detected using a long-wavelength pass filter (50% transmittance at 590 nm) with a CMOS camera (MiCAM Ultima, BrainVision, Japan; 100×100 pixel array). An electronically controlled shutter built into the light source (HL-151, Brain Vision) was set to open for 500 ms before the optical recording was triggered, as a way of avoiding mechanical disturbance caused by the shutter system and rapid bleaching of the dye.

The optical baseline was allowed to stabilize for 50 ms before delivery of any stimulus. 512 frames at a rate of 1.0ms/frame were acquired in all experiments. Color-coded optical signals were superimposed on the bright-field image to represent the spread of neural activity. The fraction of the optical signal that exceeded the baseline noise was displayed as a heatmap. Baseline noise was reduced by averaging eight identical recordings acquired with a 3s interval directly in the frame memory. The optical signals were analyzed using BrainVision analysis software. Changes in membrane potential were evaluated in a region of interest (ROI) as the fraction of change in fluorescence (dF/Fmax%), where Fmax equals the highest fluorescence value during the baseline condition of each stimulation. Based on visual inspection of the optical signal, the ROI was chosen as the region where the signal first entered the CLA. The stimulation electrode was a tungsten bipolar electrode with a tip separation of 150 μm.

A total of 28 recordings were used in these experiments. Stimulations were either elicited at a rostral position of the CL with the signal propagating in the caudal direction or at a caudal position with the signal propagating in the rostral direction. In cases where a single pulse did not elicit measurable activation in the CLA, four or five repetitive stimulations (0.1– 0.3 mA, 300 μs, 40 Hz) were used. At least five stimulation cycles were repeated for all experiments to assess if activation had occurred. Latency was measured from the beginning of the stimulus artifact to the onset of the response in the CLA. In some experiments, the recording ACSF for VSD imaging contained a low dose of 25 μM DNQX and 50 μM APV. Electrodes and parameters, as well as analyses, were based on prior studies. Following the VSD experiments, slices were postfixed in 4% PFA for up to 1 week, before being transferred to a PBS solution with 30% sucrose. Then. after at least 10 h they were

cut at 40–50 μm thickness using a freezing microtome. Sections were then mounted and Nissl-stained with Cresyl Violet before coverslipping with Entellan. Images of the sections were combined with the optical imaging data to identify the ROIs from the recordings.

Optical system for *in vivo* visualization of CLA axons

All two-photon imaging was performed using a Bruker Ultima 2P+ two-photon microscope controlled by Prairie View software, and a femtosecond-pulsed, dispersion-corrected laser (Chameleon, Coherent). Imaging was performed using a Nikon 16X 0.8NA water immersion lens. The lens was insulated from external light using a custom 3D printed cone connected to a flexible rubber sleeve. A wavelength of 920 nm and 50 mW power on sample was used for visualizing GCaMP. An imaging rate of 30Hz and a 512x512 pixel square field of view (FOV) were used for all recordings. FOVs were selected across the right side of the cranial window. The approximate coordinates of the center of the FOV relative to bregma ranged from: AP -1.2 mm to +1.3 mm; ML +0.3 mm to +1.5 mm; DV -0.03 mm to -0.3 mm.

In vivo sensory stimulation

Once mice had completely recovered from surgery, and after allowing sufficient time for viral expression (> 3 weeks), mice were assessed for GCaMP7b labeled axons in the cortex. Animals were first acclimated to head fixation under the microscope. Next, GCaMP7b expression levels were assessed by eye. Animals in which no GCaMP7b labeled axons could be found in the cranial window were excluded from future experiments. Animals with GCaMP7b labeled axons in the cortex were then used for multimodal stimulation experiments.

Sensory stimuli were delivered using a data acquisition card (National Instruments) and PackIO software. Briefly, custom MATLAB (MathWorks) code was used to generate voltage traces. These traces were then used by PackIO to output timed voltage from the data acquisition card to a white light LED (Thorlabs), a piezoelectric whisker stimulator (Physik Instrumente), and a speaker (Dell). Stimuli lasted 500ms. A complex tone, white LED light, and an oscillating paddle adjacent to the whisker pad were used for auditory, visual, and tactile stimulation respectively. The light stimulus consisted of a flash of white light, the auditory stimulus of a complex sound, and the tactile stimulus of a paddle moving vertically within the mouse's right whiskers.

During each experiment, mice were first head-fixed under the microscope. Imaging was performed in an enclosed hood to minimize visual stimuli, and white noise was used to obscure extraneous sounds. The surface of the cranial window was leveled relative to the imaging plane using a tip-tilt stage (Thorlabs). During each imaging session, FOVs with visible axon expression were selected manually. In the unimodal-only cohort (**Supp. Fig. S12**), mice were presented with 60 randomly interleaved stimulus presentations separated by randomly generated 8-11 second inter-trial intervals. These 60 stimuli were randomly drawn from 4 trial types: sound, light, whisker, and blank. In the uni- and multimodal cohort, mice were presented with 120 stimuli randomly drawn from 8 trial types: sound alone; light alone; whisker alone; sound and light; sound and whisker; light and whisker; sound, light, and whisker; and blank. During blank trials, no stimuli were delivered. The order and the precise number of each trial type were randomly generated each day. After all stimuli were delivered, a new FOV was then selected and the sensory stimulation was repeated. Imaging FOVs were selected based on visible axon expression and were drawn from across the extent of the cranial window. Care was taken to avoid recording from the same axon twice on a given day. However, as axons were only visible when active, and given the contorted and branched shape, separate regions of interest may have included the same axons.

The first round of unimodal data collection involved 5 mice (**Supp. Fig. S11** M1–4), of which 1 was excluded due to unrecoverable histology (not shown). The second round of data collection involved 7 mice (**Supp. Fig. S11** M4–9), of which 1 was excluded due to unrecoverable histology (not shown), and two were excluded due to off target expression in cortex (**Supp. Fig. S11** M8–9). Two animals were used in both data sets (**Supp. Fig. S11** M4) of which one was excluded due to unrecoverable histology (not shown).

Data Analysis & Availability

All analyses were performed with custom routines using Python 3.7.9 and open source packages unless otherwise stated. All processed data and the functions used to generate the figure panels in this study are available upon request from the authors and will be publicly available upon publication.

Electrophysiological analysis

Intrinsic electrophysiological recordings taken in current-clamp mode were passed through a series of automated quality-controls before features were calculated and stored for later cell-typing analysis. All extracted feature data is available from the authors upon request.

Neurons that passed quality-controls were first sorted manually based on their intrinsic profiles at threshold and 2x threshold current injection. Excitatory and inhibitory neurons were segregated then independently classified

into further subgroups. Automated classification involved a preprocessing step in which the electrophysiological dataset was standardized for every feature and cell. Principal component analysis (PCA) was then used to reduce the dimensionality of the standardized dataset, producing a neurons $\times$ components matrix. All components were used in uniform manifold approximation and projection (UMAP), the data from which was plotted and clustered using k-means clustering. Clusters were compared via silhouette analysis and the average silhouette score across samples was used as an indicator of how well unsupervised methods had identified which value of k best represented electrophysiological groups.

Due to poor separation among subclasses of excitatory neurons using the above method, we compared manually sorted groups of excitatory neurons using a select set of electrophysiological features. Feature comparisons for which the correlation between the features was high (r > 0.7; e.g. spike rise time and spike rise rate) were ignored for this analysis.

For *in vitro* optogenetic mapping experiments, ten trials for each cell were taken and averaged. Response magnitudes relative to baseline were calculated as the difference in the integral of the post-stimulus (30 ms after stimulus offset) and pre-stimulus (30 ms before stimulus onset) periods. Significant responses in current-clamp and voltage-clamp modes were taken as those exceeding three and five standard deviations from the average baseline period, respectively, and validated manually and by Mann-Whitney U tests that were corrected for multiple comparisons via Benjamini-Hochberg false discovery rate analysis with an alpha of 10% (**Supp. Fig. S6**, **Supp. Fig. S9**). Latencies for significant and non-significant responses were found manually. Neurons with evoked spike latencies shorter than 3 ms were taken to be directly expressing opsin and were removed from analysis **(Supp. Fig. S6)**.

Expected probabilities were defined as:

$$p(expected) = p(event_1 + event_{1+2}) * p(event_2 + event_{1+2}) \quad \textbf{(1)}$$

Morphological reconstruction analysis

Images of filled neurons were processed using ImageJ (v1.8.0_172), then uploaded to the software Neurolucida 360 (MBF) and used as a template for semi-automated, user-guided reconstruction in three dimensions. Neurolucida Explorer (MBF Bioscience) was used to extract a range of dendritic, somatic, and axonal properties from neuronal reconstructions. All cell data was compiled into an online morphological dataset that is available from the authors upon request.

Two-photon calcium imaging analysis

Calcium imaging data was preprocessed using Suite2P to automatically segment axonal regions of interest (ROIs) (83). For the unimodal-only cohort, axonal regions of interest (ROIs) were selected by hand using ImageJ. For the uni- and multimodal cohort, axonal ROIs were automatically selected using Suite2P. Automatically generated ROIs were then curated manually. ROIs were selected based on their morphology and activity traces. We computed $\Delta F/F$ for each axon using the equation:

$$\Delta F/F = (F - \bar{F})/\bar{F} \quad \textbf{(2)}$$

where: $\bar{F}$ = The mean of F across time through the entire session.

For axonal ROIs selected by suite2P, *F* was first corrected for neuropil fluorescence by subtracting 0.7*F_{Neu}. After calcium traces were exported from Suite2P, all analyses were carried out using custom MATLAB code. Calcium traces were plotted using the gramm software package (84).

Extracted calcium signals were then analyzed to identify axon segments that significantly responded to one or more sensory modalities. First, the calcium signal from 2 seconds before to 6 seconds after stimulus onset was averaged for all presentations of a given trial type (i.e. whisker alone, whisker and sound) for each axon segment in each FOV. Significantly responsive axon segments were identified by using a non-parametric Mann-Whitney U test to compare the signal in the 1 second before and after stimulus onset. Multiple comparisons correction was performed using the Benjamini-Hochberg false discovery rate analysis with an alpha of 1%.

Confocal image analysis

All images used for quantitative analysis in this study were imaged on a confocal microscope at 10X magnification (see Immunohistochemistry & imaging section above for details). Cell counts and cell coordinates were collected and analyzed using ImageJ and custom JavaScript macros. Comparisons between cell counts from injection sites were done using Mann-Whitney U tests, corrected for multiple comparisons by Bonferroni correction. Intercell distances were calculated as the smallest euclidean distance between cell somas.

Contours generated from confocal images of CTB+ neurons in the CLA (n = 3 mice) were made via morphological snakes (85, 86) of average images. Briefly, confocal images of the CLA taken from 50 μm-thick sections were thresholded using Otsu's method (87). A binary erosion algorithm (88) was applied to thresholded images to remove noise from small, punctate autofluorescence above threshold in each image. Processed images were then multiplied by their original counterparts to create denoised, native fluorescence intensity images of CTB+ CLA neurons. Images of the same slice across mice were grouped based on the Paxinos & Franklin Brain Atlas and the Allen Brain

Atlas (33, 36). Each image in a group representing a single coronal plane was normalized and aligned to the center of mass (COM) of fluorescence before being averaged into a single image. After generation of these average images for each AP plane, the border of the CLA as defined by CTB+ neurons was found by initializing an ellipse about the COM of CLA fluorescence to act as a boundary for morphological snake active contours. These contours evolve in time and are pulled toward object boundaries until the energy functions reach their minimum. Area for each contour was calculated as the integral for the closed contour path.

Confocal images of cortical axons innervating the CLA were prepared as above and COM-aligned to the CTB signal in the CLA across mice for a given cortical injection (n = 3 mice/injection site). Axonal fluorescence from each image was normalized and averaged to 15 μm$\times$15 μm bins and displayed as a heatmap.

To determine the amount of dorsal/core/ventral fluorescence within the CLA of each injection experiment, the CLA contour at the AP position of the analyzed image was used as a mask for the core. Dorsal and ventral masks were taken as the regions in the image above and below the core, including medial and lateral regions above and below ½ the core height. Image masks were multiplied to each processed and normalized image within an injection experiment set and fluorescence from that region was averaged pixel-wise. Regional fluorescence was then averaged across mice to obtain a comparison of dorsal, core, and ventral axon fluorescence in the CLA from each cortical area. Values for each region were compared using independent t-test. Multiple comparisons correction was performed using the Benjamini-Hochberg false discovery rate analysis with an alpha of 10%.

ACKNOWLEDGEMENTS

The authors gratefully acknowledge Anna Hoeder-Suabedissen, Huriye Atligan, Andrew J. King, Colin Akerman, Peter Magill, Zoltan Molnar, Armin Lak, and Christof Koch for their intellectual insights and discussion in the completion of this project. The authors also thank the Micron Advanced Bioimaging Unit (supported by Wellcome Strategic Awards 091911/B/10/Z and 107457/Z/15/Z) for their support & assistance in this work.

Funding for this work comes from the Wellcome Trust to A.M.P., the European Research Council (ERC) under the European Union's Horizon 2020 research and innovation programme (grant agreement No 852765) to A.M.P., Natural Sciences and Engineering Research Council of Canada (NSERC) to D.K.O. and Clarendon Fund graduate scholarships to A.M.S and D.K.O.

Author contributions

Conceptualization: A.M.P and A.M.S designed this study. Writing: A.M.S, S.J.B.B, and A.M.P wrote the paper with input from all coauthors. Data: A.M.S collected the data with major contributions from D.K.O and J.S.G. Further contributions to the data were made by I.P.L, I.K, A.R, J.A.S, C.A.A, S.N.W, N.C, and M.P.W. Funding Acquisition: A.M.P acquired the funding for this study. Resources: Resources were shared by A.M.P and S.J.B.B. Supervision: A.M.P and S.J.B.B supervised the work.

References

1. Kimiya Narikiyo, Rumiko Mizuguchi, Ayako Ajima, et al. The claustrum coordinates cortical slow-wave activity. *Nature Neuroscience*, 23(6):741–753, 2020.
2. Hiroaki Norimoto, Lorenz A. Fenk, Hsing Hsi Li, et al. A claustrum in reptiles and its role in slow-wave sleep. *Nature*, 578(7795):413–418, 2020.
3. Brian N. Mathur. The claustrum in review. *Frontiers in Systems Neuroscience*, 8:1–11, 2014.
4. Ryan Remedios, Nikos K. Logothetis, and Christoph Kayser. A role of the claustrum in auditory scene analysis by reflecting sensory change. *Frontiers in Systems Neuroscience*, 8(1 APR):1–8, 2014.
5. Francis Crick and Christof Koch. What is the function of the claustrum? *Philosophical Transactions of the Royal Society B: Biological Sciences*, 360(1458):1271–1279, 2005.
6. John Smythies, Lawrence Edelstein, and Vilayanur Ramachandran. Hypotheses relating to the function of the claustrum. *Frontiers in Integrative Neuroscience*, 6(AUGUST 2012):1–16, 2012.
7. John Smythies, Lawrence Edelstein, and Vilayanur Ramachandran. Hypotheses relating to the function of the claustrum II: Does the claustrum use frequency codes? *Frontiers in Integrative Neuroscience*, 8(JAN):2012–2014, 2014.
8. Trichur R. Vidyasagar and Ekaterina Levichkina. An integrated neuronal model of claustral function in timing the synchrony between cortical areas. *Frontiers in Neural Circuits*, 13(February):1–8, 2019.
9. Gal Atlan, Noa Matosevich, Noa Peretz-Rivlin, et al. Claustral Projections to Anterior Cingulate Cortex Modulate Engagement with the External World. *bioRxiv* 2021.06.17.448649, 2021.
10. Leon Fodoulian, Olivier Gschwend, Chieko Huber, et al. The claustrum-medial prefrontal cortex network controls attentional set-shifting. *bioRxiv* 2020.10.14.339259, 2020.
11. Christopher M. Dillingham, Maciej M. Jankowski, Ruchi Chandra, et al. The claustrum: Considerations regarding its anatomy, functions and a programme for research. *Brain and Neuroscience Advances*, 1, 2017.
12. Jesse Jackson, Jared B. Smith, and Albert K. Lee. The Anatomy and Physiology of Claustrum-Cortex Interactions. *Annual Review of Neuroscience*, 43(1):231–247, July 2020.
13. Yael Goll, Gal Atlan, and Ami Citri. Attention: The claustrum. *Trends in Neurosciences*, 38(8):486–495, 2015.
14. Huriye Atilgan, Max Doody, David K Oliver, et al. Human leisions and animal studies links the claustrum to perception, salience, sleep, and pain. *Brain*, 2022.
15. L. R. Edelstein and F. J. Denaro. The claustrum: a historical review of its anatomy, physiology, cytochemistry and functional significance. *Cellular and molecular biology*, 50(6):675–702, 2004.
16. Maria Cristina Patru and David H. Reser. A new perspective on delusional states - Evidence for claustrum involvement. *Frontiers in Psychiatry*, 6(November):1–14, 2015.
17. Brian Zingg, Houri Hintiryan, Lin Gou, et al. Neural networks of the mouse neocortex. *Cell*, 156(5):1096–1111, 2014.
18. Gal Atlan, Anna Terem, Noa Peretz-Rivlin, et al. Mapping synaptic cortico-claustral connectivity in the mouse. *Journal of Comparative Neurology*, 525(6):1381–1402, 2017.
19. Hanchuan Peng, Peng Xie, Lijuan Liu, et al. Brain-wide single neuron reconstruction reveals morphological diversity in molecularly defined striatal, thalamic, cortical and claustral neuron types. *bioRXiv*, June 2019.
20. Quanxin Wang, Yun Wang, Peng Xie, et al. Regional and cell type-specific afferent and efferent projections of the mouse claustrum. *bioRXiv*, 2022.
21. Zach Chia, George J. Augustine, and Gilad Silberberg. Synaptic Connectivity between the Cortex and Claustrum Is Organized into Functional Modules. *Current Biology*, 30(14):2777–2790.e4, July 2020.
22. Brian A. Marriott, Alison D. Do, Ryan Zahacy, and Jesse Jackson. Topographic gradients define the projection patterns of the claustrum core and shell in mice. *Journal of Comparative Neurology*, 529(7):1607–1627, 2021.
23. Maxime Chevée, Eric A. Finkel, Su-Jeong Kim, et al. Neural activity in the mouse claustrum in a cross-modal sensory selection task. *Neuron*, 110(3):486–501.e7, February 2022.
24. Martin Graf, Aditya Nair, Kelly L.L. Wong, et al. Identification of mouse claustral neuron types based on their intrinsic electrical properties. *eNeuro*, 7(4):1–29, 2020.
25. Juhyun Kim, Chanel J. Matney, Richard H. Roth, and Solange P. Brown. Synaptic organization of the neuronal circuits of the claustrum. *Journal of Neuroscience*, 36(3):773–784, 2016.
26. S. LeVay and H. Sherk. The visual claustrum of the cat. I. Structure and connections. *Journal of Neuroscience*, 1(9):956–980, 1981.
27. J. B. Smith and K. D. Alloway. Functional Specificity of Claustrum Connections in the Rat: Interhemispheric Communication between Specific Parts of Motor Cortex. *Journal of Neuroscience*, 30(50):16832–16844, December 2010.
28. J. B. Smith, H. Radhakrishnan, and K. D. Alloway. Rat Claustrum Coordinates But Does Not Integrate Somatosensory and Motor Cortical Information. *Journal of Neuroscience*, 32(25):8583–8588, June 2012.
29. Tifei Yuan, Adam M. Packer, N. Pettit, et al. Integration of multisensory inputs by single neurons in the claustrum. *Society for Neuroscience Annual Meeting*, 2015.
30. Houman Qadir, Brent W. Stewart, Jonathan Van Ryzin, et al. The mouse claustrum synaptically connects cortical network motifs. *bioRXiv*, April 2022.
31. Ryan Remedios, Nikos K. Logothetis, and Christoph Kayser. Unimodal responses prevail within the multisensory claustrum. *Journal of Neuroscience*, 30(39):12902–12907, 2010.
32. Brian Zingg, Hong Wei Dong, Huizhong Whit Tao, and Li I. Zhang. Input–output organization of the mouse claustrum. *Journal of Comparative Neurology*, 526(15):2428–2443, 2018.
33. Keith B. J. Franklin and George Paxinos. *The mouse brain in stereotaxic coordinates*, Amsterdam, 3. ed edition, 2008.

34. Joachim S. Grimstvedt, Andrew M. Shelton, Anna Hoerder-Suabedissen, et al. A multi-faceted architectural definition of the mouse claustrum complex. *in preparation*, 2022.
35. Quanxin Wang, Lydia Ng, Julie A. Harris, et al. Organization of the connections between claustrum and cortex in the mouse. *Journal of Comparative Neurology*, 525(6):1317–1346, 2017.
36. Quanxin Wang, Song Lin Ding, Yang Li, et al. The Allen Mouse Brain Common Coordinate Framework: A 3D Reference Atlas. *Cell*, 181(4):936–953.e20, 2020.
37. Rastislav Druga, Sheng Chen, and Marina Bentivoglio. Parvalbumin and calbindin in the rat claustrum: An immunocytochemical study combined with retrograde tracing from frontoparietal cortex. *Journal of Chemical Neuroanatomy*, 6(6):399–406, 1993.
38. Ma Ángeles Real, José Carlos Dávila, and Salvador Guirado. Expression of calcium-binding proteins in the mouse claustrum. *Journal of Chemical Neuroanatomy*, 25(3):151–160, 2003.
39. Ma Ángeles Real, José Carlos Dávila, and Salvador Guirado. Immunohistochemical localization of the vesicular glutamate transporter VGLUT2 in the developing and adult mouse claustrum. *Journal of Chemical Neuroanatomy*, 31(3):169–177, 2006.
40. Simon J.B. Butt, Marc Fuccillo, Susana Nery, et al. The temporal and spatial origins of cortical interneurons predict their physiological subtype. *Neuron*, 48(4):591–604, 2005.
41. Yasuo Kawaguchi and Yoshiyuki Kubota. GABAergic cell subtypes and their synaptic connections in rat frontal cortex. *Cerebral Cortex*, 7(6):476–486, 1997.
42. Rena Orman. Claustrum: a case for directional, excitatory, intrinsic connectivity in the rat. *Journal of Physiological Sciences*, 65(6):533–544, 2015.
43. Jared B. Smith and Kevin D. Alloway. Interhemispheric claustral circuits coordinate sensory and motor cortical areas that regulate exploratory behaviors. *Frontiers in Systems Neuroscience*, 8(MAY):1–14, 2014.
44. Leopoldo Petreanu, Daniel Huber, Aleksander Sobczyk, and Karel Svoboda. Channelrhodopsin-2-assisted circuit mapping of long-range callosal projections. *Nature Neuroscience*, 10(5):663–668, 2007.
45. Sarah Melzer, Magdalena Michael, Antonio Caputi, et al. Long-Range–Projecting GABAergic Neurons Modulate Inhibition in Hippocampus and Entorhinal Cortex. *Science*, 335(March):1506–1511, 2012.
46. Yiding Li, Jiamin Xu, Yafeng Liu, et al. A distinct entorhinal cortex to hippocampal CA1 direct circuit for olfactory associative learning. *Nature Neuroscience*, 20(4):559–570, April 2017.
47. Joel Bauer, Simon Weiler, Martin H.P. Fernholz, et al. Limited functional convergence of eye-specific inputs in the retinogeniculate pathway of the mouse. *Neuron*, 109(15):2457–2468.e12, August 2021.
48. Bryan M. Hooks, John Y. Lin, Caiying Guo, and Karel Svoboda. Dual-channel circuit mapping reveals sensorimotor convergence in the primary motor cortex. *Journal of Neuroscience*, 35(10):4418–4426, 2015.
49. Maxime Chevée, Eric A. Finkel, Su-Jeong Kim, et al. Neural activity in the mouse claustrum in a cross-modal sensory selection task. *Neuron* 1–16, 2021.
50. Douglas R Ollerenshaw, Julianne Davis, Ethan G McBride, et al. Anterior claustrum cells are responsive during behavior but not passive sensory stimulation. *bioRxiv* 2021.03.23.436687, 2021.
51. Ethan G. McBride, Saurabh R. Gandhi, Jacqulyn R. Kuyat, et al. Influence of claustrum on cortex varies by area, layer, and cell type. *bioRxiv* 1–25, 2022.
52. Sarah R. Erwin, Brianna N. Bristow, Kaitlin E. Sullivan, et al. Spatially patterned excitatory neuron subtypes and circuits within the claustrum. *bioRxiv*, 2021.
53. Rastislav Druga. The Structure and Connections of the Claustrum. In *The Claustrum: Structural, Functional, and Clinical Neuroscience* 29–84, 2014.
54. S. LeVay. Synaptic organization of claustral and geniculate afferents to the visual cortex of the cat. *Journal of Neuroscience*, 6(12):3564–3575, 1986.
55. H. Shibuya and T. Yamamoto. Electrophysiological and morphological features of rat claustral neurons: An intracellular staining study. *Neuroscience*, 85(4):1037–1049, 1998.
56. Laura M. McGarry, Adam M. Packer, Elodie Fino, et al. Quantitative classification of somatostatin-positive neocortical interneurons identifi es three interneuron subtypes. *Frontiers in Neural Circuits*, 4(May):1–19, 2010.
57. Maria Toledo-Rodriguez, Barak Blumenfeld, Caizhi Wu, et al. Correlation maps allow neuronal electrical properties to be predicted from single-cell gene expression profiles in rat neocortex. *Cerebral Cortex*, 14(12):1310–1327, 2004.
58. B. Spahn and H. Braak. Percentage of projection neurons and various types of interneurons in the human claustrum. *Cells Tissues Organs*, 122(4):245–248, 1985.
59. Nathan W. Gouwens, Staci A. Sorensen, Jim Berg, et al. Classification of electrophysiological and morphological neuron types in the mouse visual cortex. *Nature Neuroscience*, 22(7):1182–1195, 2019.
60. Bernardo Rudy, Gordon Fishell, Soo Hyun Lee, and Jens Hjerling-Leffler. Three groups of interneurons account for nearly 100% of neocortical GABAergic neurons. *Developmental Neurobiology*, 71(1):45–61, 2011.
61. Jayeeta Basu, Jeffrey D. Zaremba, Stephanie K. Cheung, et al. Gating of hippocampal activity, plasticity, and memory by entorhinal cortex long-range inhibition. *Science*, 351(6269):aaa5694, January 2016.
62. Jacqueline Boon, Emma Clarke, Nicoletta Kessaris, et al. Long-range projections from sparse populations of GABAergic neurons in murine subplate. *Journal of Comparative Neurology*, 527(10):1610–1620, 2019.
63. Shozo Jinno, Thomas Klausberger, Laszlo F. Marton, et al. Neuronal diversity in GABAergic long-range projections from the hippocampus. *Journal of Neuroscience*, 27(33):8790–8804, 2007.
64. Anthony T. Lee, Daniel Vogt, John L. Rubenstein, and Vikaas S. Sohal. A class of GABAergic neurons in the prefrontal cortex sends long-range projections to the nucleus accumbens and elicits acute avoidance behavior. *Journal of Neuroscience*, 34(35):11519–11525, 2014.
65. Sarah Melzer and Hannah Monyer. Diversity and function of corticopetal and corticofugal GABAergic projection neurons. *Nature Reviews Neuroscience* 17, 2020.
66. Zoltán Molnár and Ann B. Butler. Neuronal changes during forebrain evolution in amniotes: an evolutionary developmental perspective. In *Progress in Brain Research*, volume 136 21–38, 2002.
67. Hannah Bruguier, Rodrigo Suarez, Paul Manger, et al. In search of common developmental and evolutionary origin of the claustrum and subplate. *Journal of Comparative Neurology*, 528(17):2956–2977, 2020.
68. G. A. Calvert. Crossmodal Processing in the Human Brain: Insights from Functional Neuroimaging Studies. *Cerebral Cortex*, 11(12):1110–1123, December 2001.
69. G. Ettlinger and W.A. Wilson. Cross-modal performance: behavioural processes, phylogenetic considerations and neural mechanisms. *Behavioural Brain Research*, 40(3):169–192, November 1990.
70. Michael G. White, Matthew Panicker, Chaoqi Mu, et al. Anterior Cingulate Cortex Input to the Claustrum Is Required for Top-Down Action Control. *Cell Reports*, 22(1):84–95, 2018.
71. S. LeVay and H. Sherk. The visual claustrum of the cat. II. The visual field map. *Journal of Neuroscience*, 1(9):981–992, 1981.
72. C. R. Olson and A. M. Greybiel. Sensory maps in the claustrum of the cat. *Nature*, 1980.
73. Gal Atlan, Anna Terem, Noa Peretz-Rivlin, et al. The Claustrum Supports Resilience to Distraction. *Current Biology*, 28(17):2752–2762.e7, 2018.
74. Jesse Jackson, Mahesh M. Karnani, Boris V. Zemelman, et al. Inhibitory Control of Prefrontal Cortex by the Claustrum. *Neuron*, 99(5):1029–1039.e4, 2018.
75. R. Cortimiglia, G. Crescimanno, M.T. Salerno, and G. Amato. The role of the claustrum in the bilateral control of frontal oculomotor neurons in the cat. *Experimental Brain Research*, 84(3), April 1991.
76. Tadaharu Tsumoto and Kouhei Suda. Effects of stimulation of the dorsocaudal claustrum on activities of striate cortex neurons in the cat. *Brain Research* 5, 1982.
77. Randy M Bruno. Synchrony in sensation. *Current Opinion in Neurobiology*, 21(5):701–708, October 2011.
78. Micah M. Murray and Mark T. Wallace. *The Neural Bases of Multisensory Processes*, 1 edition, August 2011.
79. Stefan Blankvoort, Lucie A.L. Descamps, and Cliff Kentros. Enhancer-Driven Gene Expression (EDGE) enables the generation of cell type specific tools for the analysis of neural circuits. *Neuroscience Research*, 152:78–86, March 2020.
80. Rajeevkumar Raveendran Nair, Stefan Blankvoort, Maria Jose Lagartos, and Cliff Kentros. Enhancer-Driven Gene Expression (EDGE) Enables the Generation of Viral Vectors Specific to Neuronal Subtypes. *iScience*, 23(3):100888, March 2020.
81. D. Gowanlock R. Tervo, Bum Yeol Hwang, Sarada Viswanathan, et al. A Designer AAV Variant Permits Efficient Retrograde Access to Projection Neurons. *Neuron*, 92(2):372–382, 2016.
82. Brendon O Watson, Rafael Yuste, and Adam M Packer. PackIO and EphysViewer: software tools for acquisition and analysis of neuroscience data. *bioRXiv* 29, 2016.
83. Marius Pachitariu, Carsen Stringer, Mario Dipoppa, et al. Suite2p: beyond 10,000 neurons with standard two-photon microscopy. preprint, Neuroscience, June 2016.
84. Pierre Morel. Gramm: grammar of graphics plotting in Matlab. *The Journal of Open Source Software*, 3(23):568, March 2018.
85. V. Caselles, R. Kimmel, and G. Sapiro. Geodesic active contours. *Proceedings of IEEE International Conference on Computer Vision* 694–699, 1995.
86. Michael Kass, Andrew Witkin, and Demetri Terzopoulos. Snakes: Active contour models. *International Journal of Computer Vision*, 1(4):321–331, 1988.
87. Nobuyuki Otsu. A Threshold Selection Method from Gray-Level Histograms. *IEEE Transactions on Systems, Man, and Cybernetics*, C(1):62–66, 1979.
88. Rafael C. Gonzalez, Richard E. Woods, and Barry R. Masters. Digital Image Processing, Third Edition. *Journal of Biomedical Optics*, 14(2), 2009.

Cortical area	Abbreviation
Claustrum	CLA
Retrosplenial-projecting CLA	CLA_{RSP}
Retrosplenial area	RSP
Orbitofrontal area	ORB
Prelimbic area	PL
Anterior cingulate area, anterior part	ACAa
Anterior cingulate area, posterior part	ACAp
Primary motor area	MOp
Dorsal auditory area	AUDd
Anteromedial visual area	VISam
Entorhinal area, lateral part	ENTl

Table 2. Abbreviations of cortical areas used to assess corticoclaustral connectivity. From the Allen Institute Mouse Reference Atlas (see (36)).

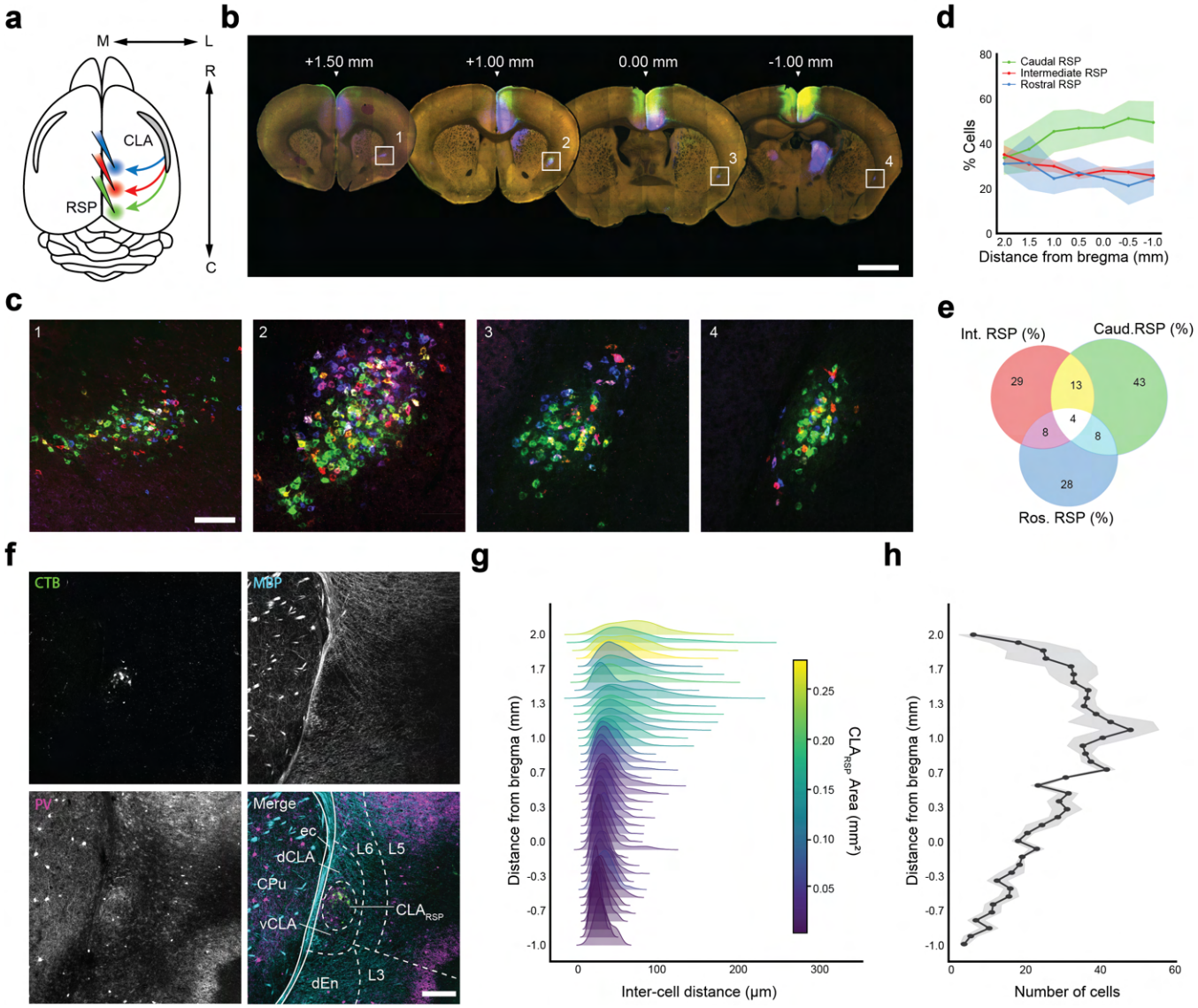

Fig. 1. Interrogation of a projection-defined CLA neuronal subpopulation. **(a)** Schematic of the injection strategy. **(b)** Representative 100 μm sections spanning the rostrocaudal axis of the brain in which the CLA can be seen retro-labeled by CTB from rostral (blue), intermediate (red), and caudal (green) injections into RSP (n = 3 mice). Scale bar = 1 mm. **(c)** Insets of **b** in which CLA neurons are labeled with CTB. Scale bar = 200 μm **(d)** Percent of counted neurons that project to different regions of RSP from per section from experiments in a-c. **(e)** Venn diagram displaying the percentage of all counted cells labeled by each injection, including double and triple-labeled cells. **(f)** Immunohistochemistry of a representative CLA section (AP = 0.0 mm bregma) against PV (magenta) and MBP (cyan) with CLA_{RSP} retro-labeled CLAneurons (green). Regional labels: CPu = caudoputamen, ec = external capsule, dCLA = dorsal CLA, vCLA = ventral CLA, DEn = dorsal endopiriform. Scale bar = 200 μm. **(g)** Probability density distributions of the euclidean distance between CLA_{RSP} neurons across the coronal axis in 50 μm sections across the rostrocaudal axis, colored by the cross-sectional area of CLA_{RSP} neurons. **(h)**: Number of cells counted in the sections from **g**, right (n = 3 mice).

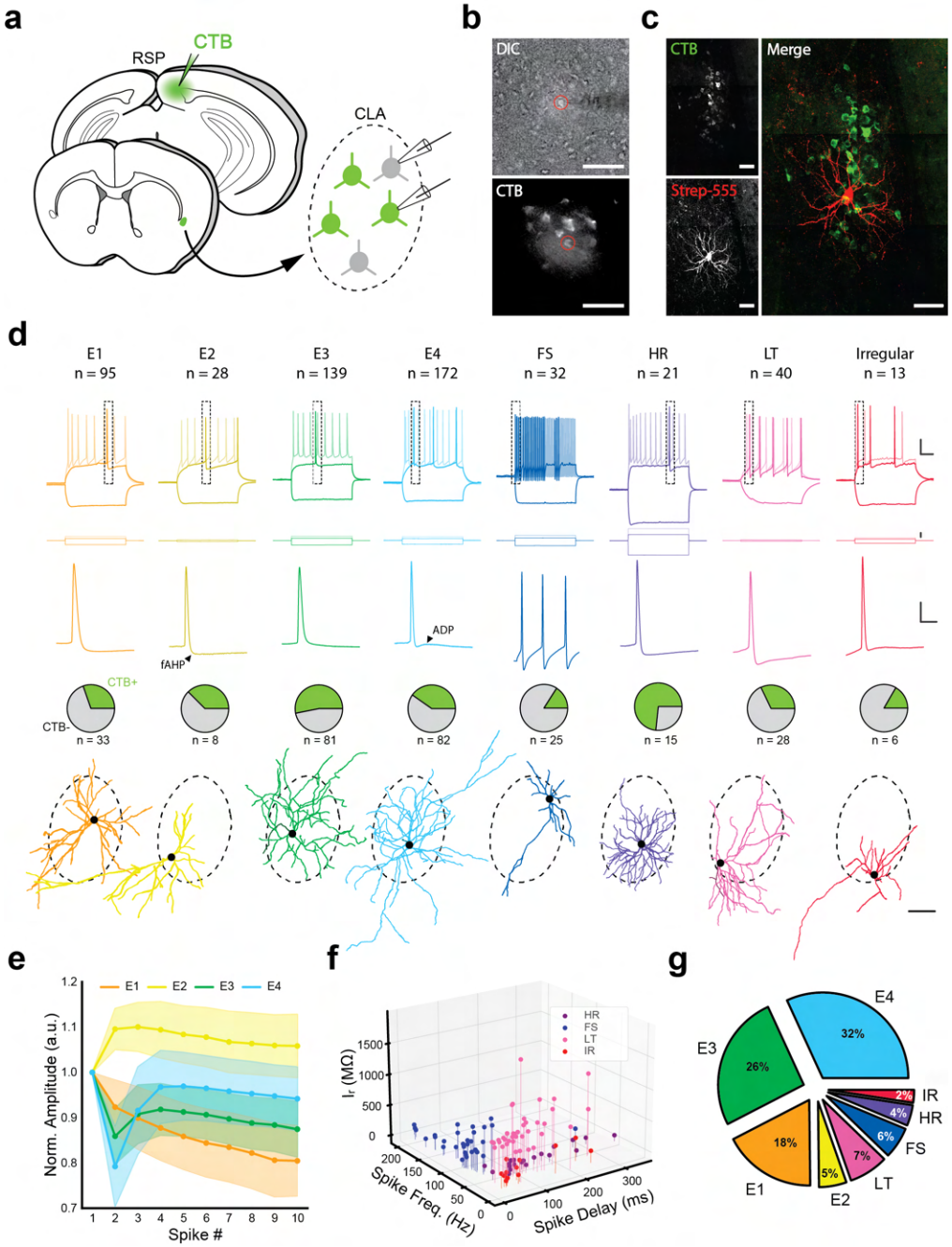

Fig. 2. Electrophysiologically-defined cell types of the CLA. **(a)** Schematic of injection and patching strategy in the CLA. **(b)** 40X DIC (top) and CTB (bottom) example images of a neuron during patching. Scale bar = 100 μm. **(c)** Confocal microscopic images of a filled neuron post-patching. Scale bar = 50 μm. **(d)** Intrinsic electrophysiological profiles, expanded spike waveforms (from top inset), proportion of neurons found to be CTB+ during experiments (cells for which CTB status was known), and example morphological reconstructions for each electrophysiological cell type. Scale bars (top to bottom): 20 mV/100 ms, 300 pA, 20 mV/10 ms, 50 μm. Dashed border around morphologies represents the average CLA_{RSP} area across slices from **Fig. 1f** and **Supp. Fig. S2**. Somas aligned to their approximate location in this region during patching. **(e)** Comparison of spike amplitude between excitatory types on the first ten spikes during 2x rheobase current injection, normalized to the amplitude of the first spike. **(f)** Comparison of features distinguishing interneuron types. **(g)**: Proportion of all patched neurons of each putative cell type (n = 540).

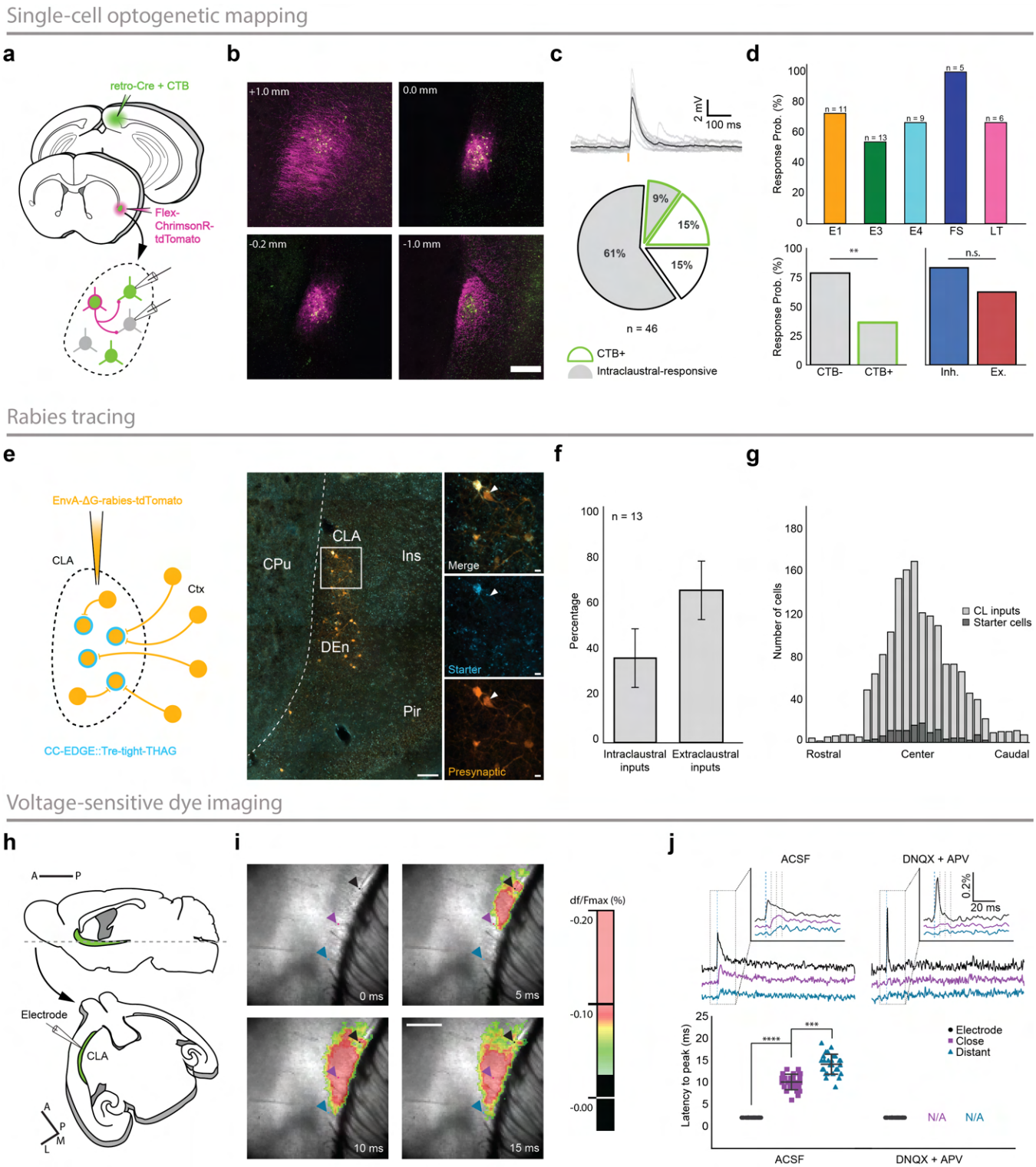

Fig. 3. Intraclaustral connectivity is common, cross-modular, and spans the rostrocaudal axis. **(a)** Schematic of injection and patching strategy in the CLA. **(b)** Expression of AAV-FLEX-ChrimsonR-tdTomato and CTB in the CLA along the rostrocaudal axis. Notice the lack of tdTomato+ cell bodies in the far rostral and far caudal sections beyond the spread of the virus. Scale bar = 200 μm. **(c)** CLA neurons frequently displayed EPSPs in response to presynaptic CLA_{RSP} neuron photostimulation with 595 nm light (top). CLA neurons not labeled with CTB were found to be proportionally the most likely to respond to presynaptic photostimulation (n = 28/46 neurons, bottom). **(d, top)** Most electrophysiological types were represented among neurons responsive to CLA input (n is the number of neurons recorded in each group, total n = 32 responsive/46 neurons). No significant difference in response probability was found between excitatory and inhibitory cell types (p = 0.29, Fisher exact test), while a significant difference in responsivity was found between CTB+ and CTB- neurons (p = 0.009, Fisher Exact Test) **(bottom)**. **(e, left)** Schematic of rabies injection strategy. **(e, right)** Light microscopy of the CLA and DEn stained for starter (cyan) and presynaptic (orange) neurons. Scale bars = 50 μm, 10 μm. **(f)** Proportion of counted presynaptic neurons found to be in the CLA and outside of the CLA (n = 13 mice, p = 0.0013). **(g)** Pooled distribution of input- (light gray) and starter-cells (dark gray), aligned to the median rostrocaudal location of each starter-population. **(h)** Schematic of VSDI experiments in horizontal sections of a rat brain. **(i)** Voltage indicator images of the CLA in response to electrical stimulation of the rostral CLA 0, 5, 10, and 15 ms after stimulation onset. Colored arrows indicate locations used for analysis in **j**. Scale bar = 1 mm. **(j)** Traces from the pixels in **i** demonstrating the delay in time to peak from rostral to caudal regions of the CLA **(top, left)**. DNQX + APV application to slices during experiments extinguished this response **(top, right)**. Quantification of the time to peak signal for each pixel in **i** and **j (top)**. Caudal pixels show a significant delay in ACSF experiments but no response when glutamatergic signaling is blocked in DNQX + APV experiments.

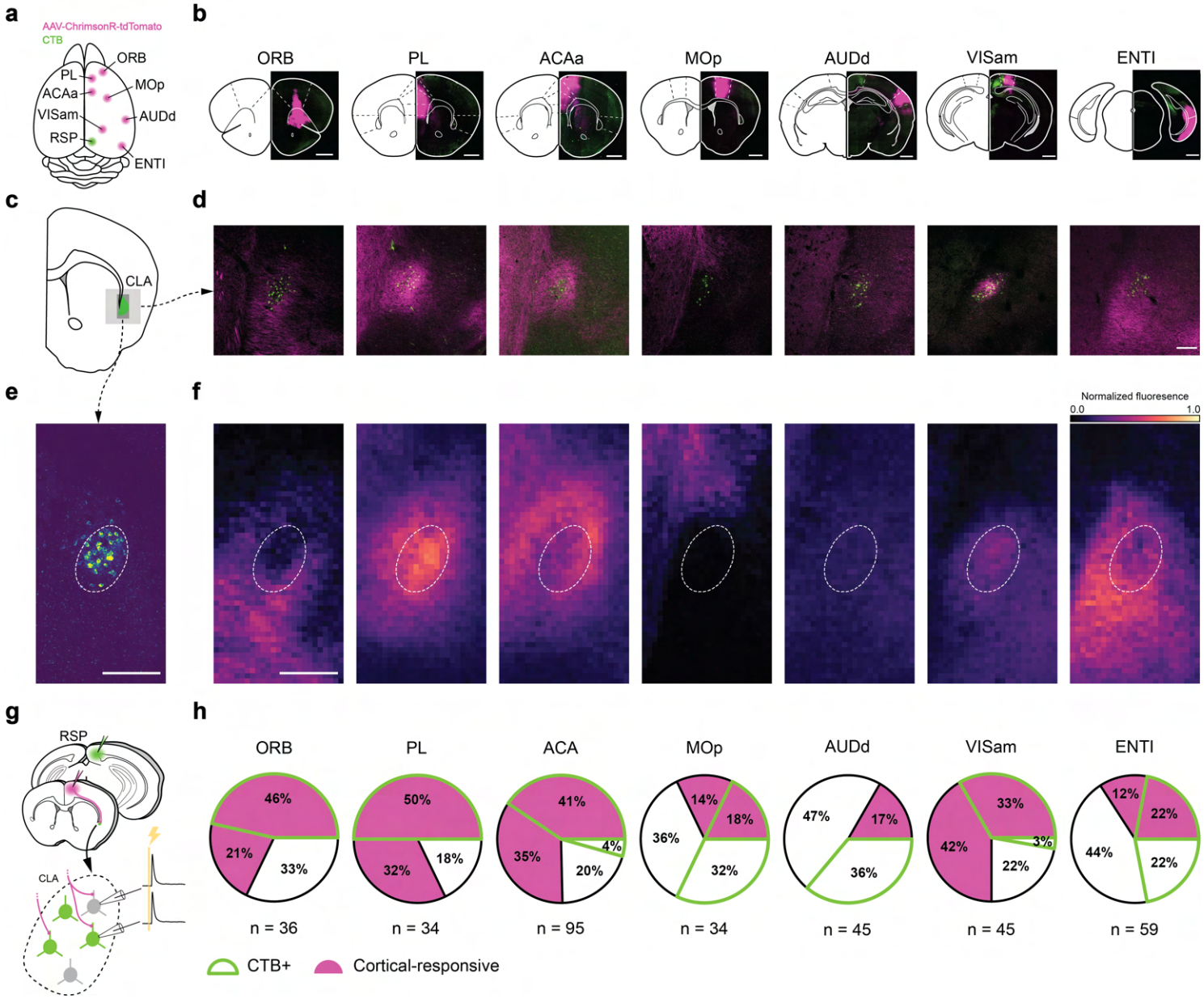

Fig. 4. Spatial distribution of afferent projections onto the CLA. (a) Schematic of injection sites in the cortex. Individual Chrimson-tdTomato (magenta) injection sites were combined with an injection of CTB (green) into the RSP. **(b)** Coronal sections of example injection sites. Scale bars = 1 mm. **(c)** Schematics of a representative section of the CLA at 1 mm rostral to bregma. **(d)** Histological sections from the representative section in **c** and each input cortical area in **b**. Scale bar = 200 μm. **(e)** Example image of CLA_{RSP} neurons overlaid with the average contour representing the CLA_{RSP} core (n = 21 mice). **(f)** Heatmaps of normalized fluorescence in corticoclaustral axons. Scale bar = 200 μm, 15 μm/pixel. **(g)** Schematic of the patching strategy used to investigate single-cortex innervation of the CLA. **(f)** Individual response and CTB proportions of CLA neurons to each cortex investigated in these experiments. CLA_{RSP} neurons were found to be the most responsive to frontal-cortical input and less responsive to inputs from other regions, with the exception of VISam.

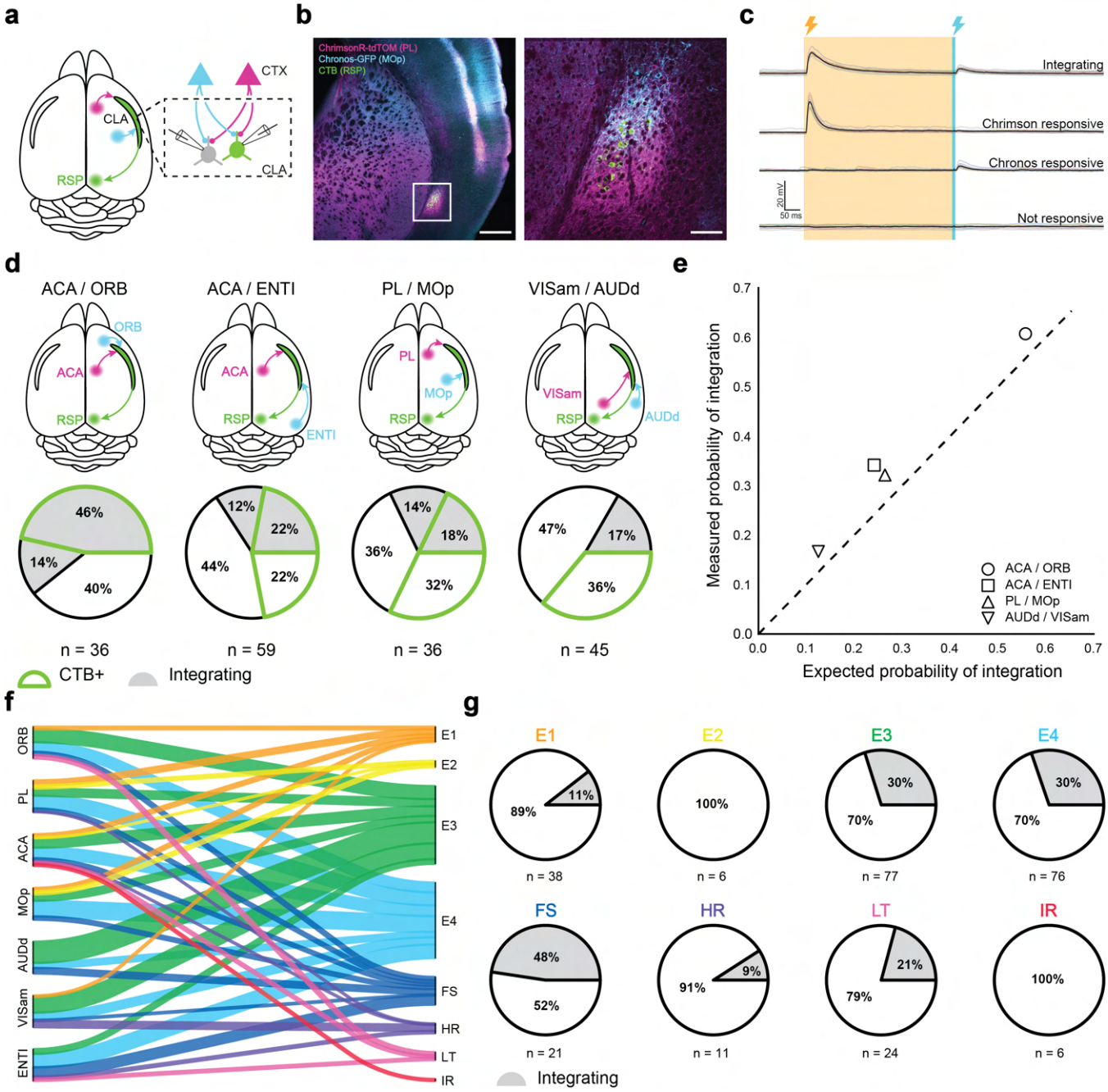

Fig. 5. Dual-color optogenetics reveals integration among CLA neurons. **(a)** Schematic of injection and patching strategy in the CLA. **(b)** Confocal images of AAV-Chrimson-tdTomato and AAV-Chronos-GFP expression in cortical axons in the CLA. Scale bars = 500 μm, 100 μm. **(c)** Example traces of different response outcomes for CLA neurons after sequential cortical axon photostimulation. From top to bottom: integrating responses indicated a neuron was responsive to both input cortices, Chrimson-responsive indicated a neuron responsive to only one cortex while Chronos-responsive indicated a neuron responsive to the other cortex. Finally, no response indicated no detectable synaptic connection. **(d)** Dual-color optogenetics response and CTB proportions for cortices examined in **Fig. 4** using the strategy in **c**. **(e)** Expected vs. measured response probabilities for neurons in each dual-color optogenetics combination. All cortical combinations displayed a slightly higher response probability than expected by chance. **(f)** River plot displaying the proportion of neurons projected to by each cortical area, categorized by cell type. **(g)** Proportion of integrating cells within each electrophysiological cell type.

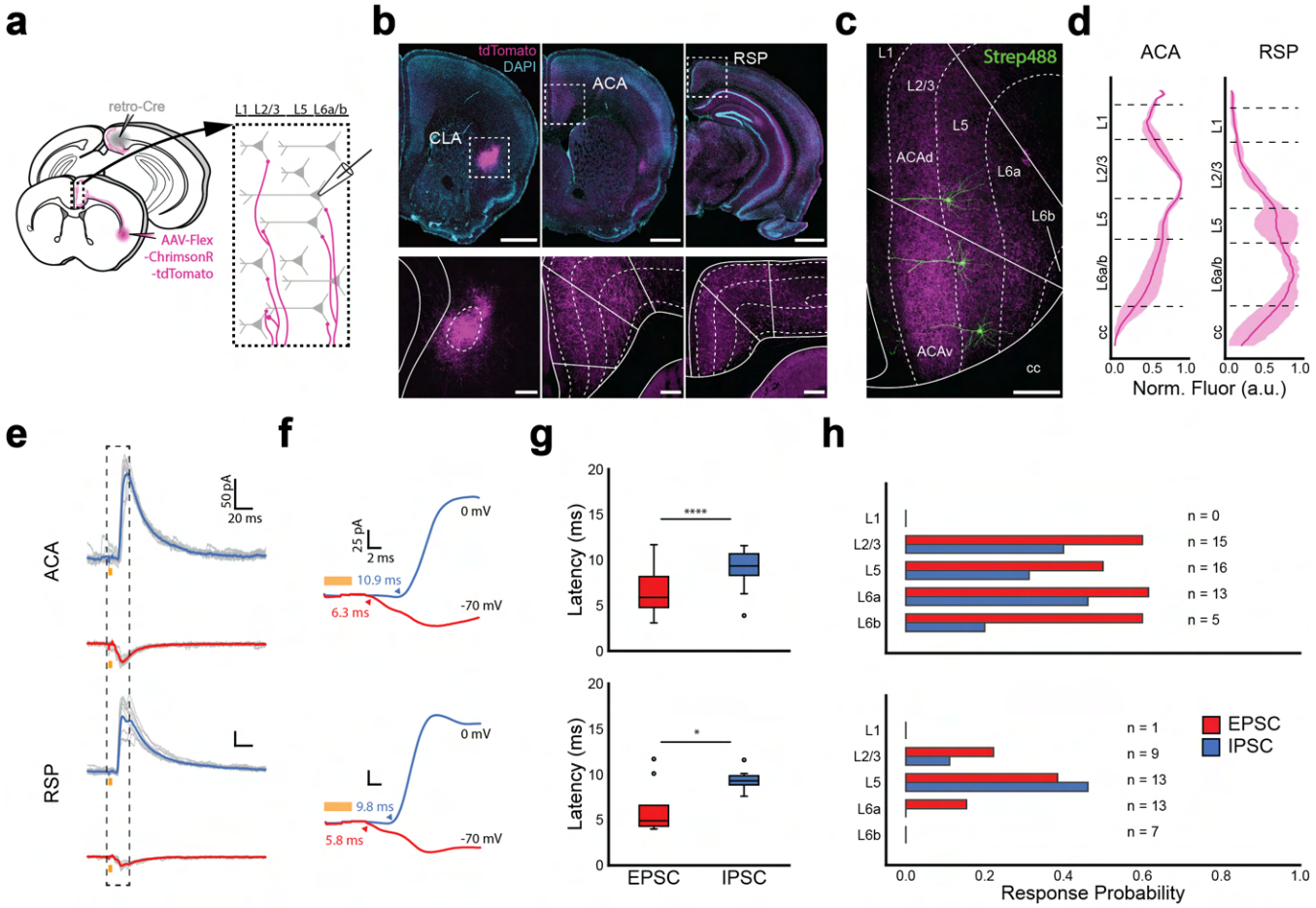

Fig. 6. CLA afferents target cortices in a layer specific fashion. **(a)** Schematic of injection and patching strategy for assessing cortex responses to photostimulation of CLA axons. **(b)** Representative coronal sections of opsin expression in CLA cell bodies (left), ACA (middle), and RSP (right). Scale bars = 1 mm (top), 200 μm (bottom). **(c)** Example image of L5 pyramidal neurons patched in L5 of ACA. Layer definitions based on the Allen Brain Atlas. Scale bar = 200 μm. **(d)** Normalized CLA axonal fluorescence in ACA and RSP. **(e)** Example traces of IPSC (0 mV, blue trace) and EPSC (-70 mV, red trace) responses from a single neuron in both the ACA and RSP. **(f)** Mean IPSCs and EPSCs from **e** aligned to stimulus onset. **(g)** EPSC and IPSC latency for ACA (top) and RSC (bottom). EPSC and IPSC latency for ACA (top) and RSC (bottom). IPSC latency than EPSC latency in each area (ACA: p = 0.0006; RSP: p = 0.025). **(h)** PSC probability in cortical neurons sorted by the layer in which neurons were patched (n = 92 cells, 10 mice).

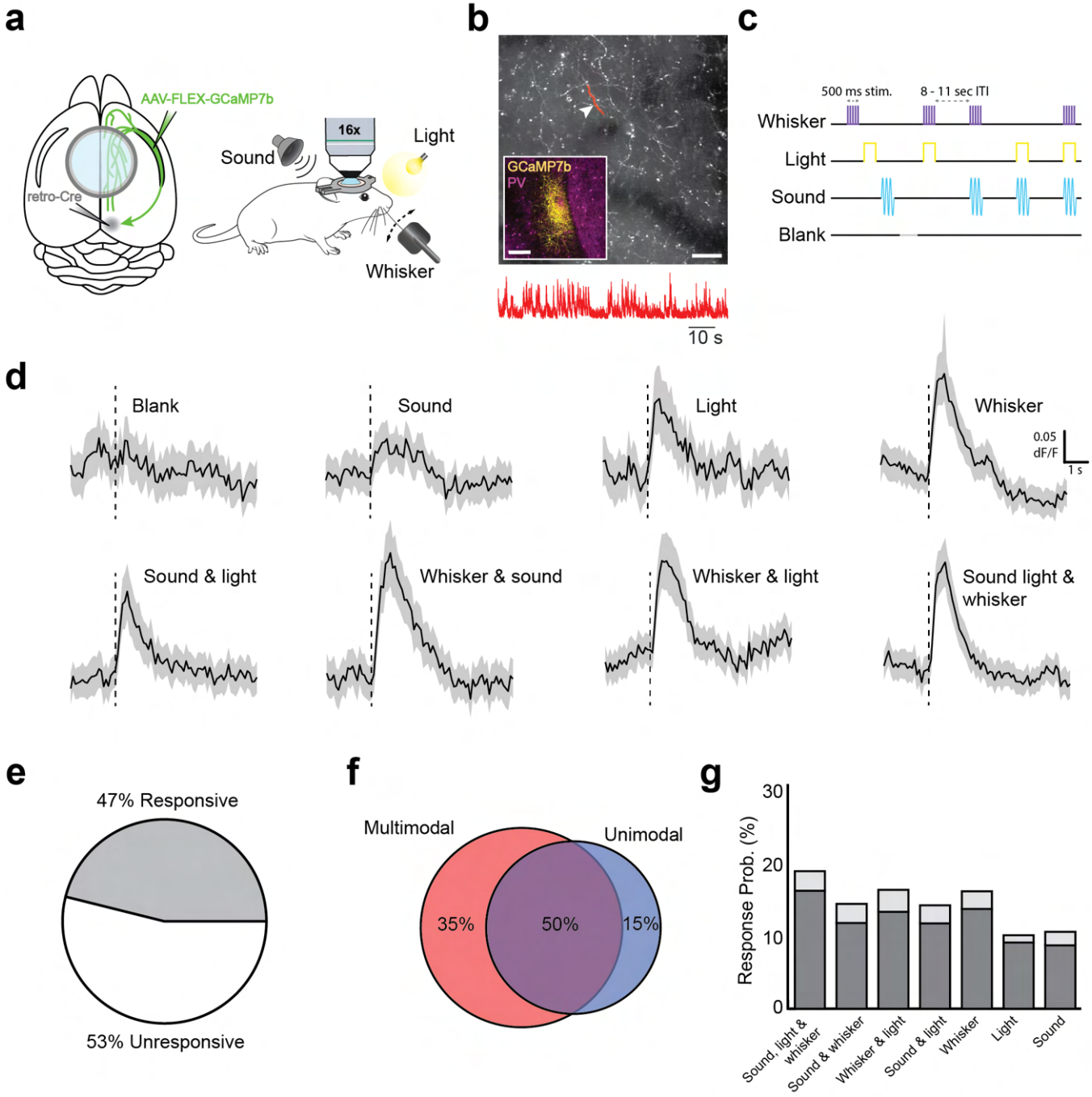

Fig. 7. ***In vivo*** **imaging of sensory-responsive CLA axons in cortex**. **(a, left)** Schematic of injection strategy and window placement over bregma. **(a, right)** Schematic of *in vivo* recording strategy with symbols for stimuli (upper right: white-noise tone, upper left: LED light, lower left: whisker stimulator). **(b)** Example FOV above ACA with CLA axons expressing GCaMP7b. Scale bar = 50 μm, 10 seconds. *Inset*: GCaMP7b expression in CLA from approximately 0.0 mm bregma. Inset scale bar = 200 μm. Highlighted area and arrow indicate the axon from which the red trace below was recorded. Scale bar = 50 μm, 10 seconds. **(c)** Passive stimulation protocol using three stimulus modalities. Stimuli and combinations thereof were presented 8-11 s apart (randomized) with a fourth "blank" period where no stimulus was presented. **(d)** Average dF/F traces for each stimulus and combination type across all axons displaying significant responses to each modality (n = 4 mice, 1364 axons). **(e)** Proportion of all recorded axons displaying responses to any of the stimuli in **d**. **(f)** Some axons were modulated only by combinations of stimuli **(left)**, both single and multiple stimuli **(center)**, or only single stimuli **(right)**. **(g)** Percentage of all significantly activated axons responsive to each category and combination of stimuli. Light gray bars show the percentage exclusively responsive to each stimulus type.

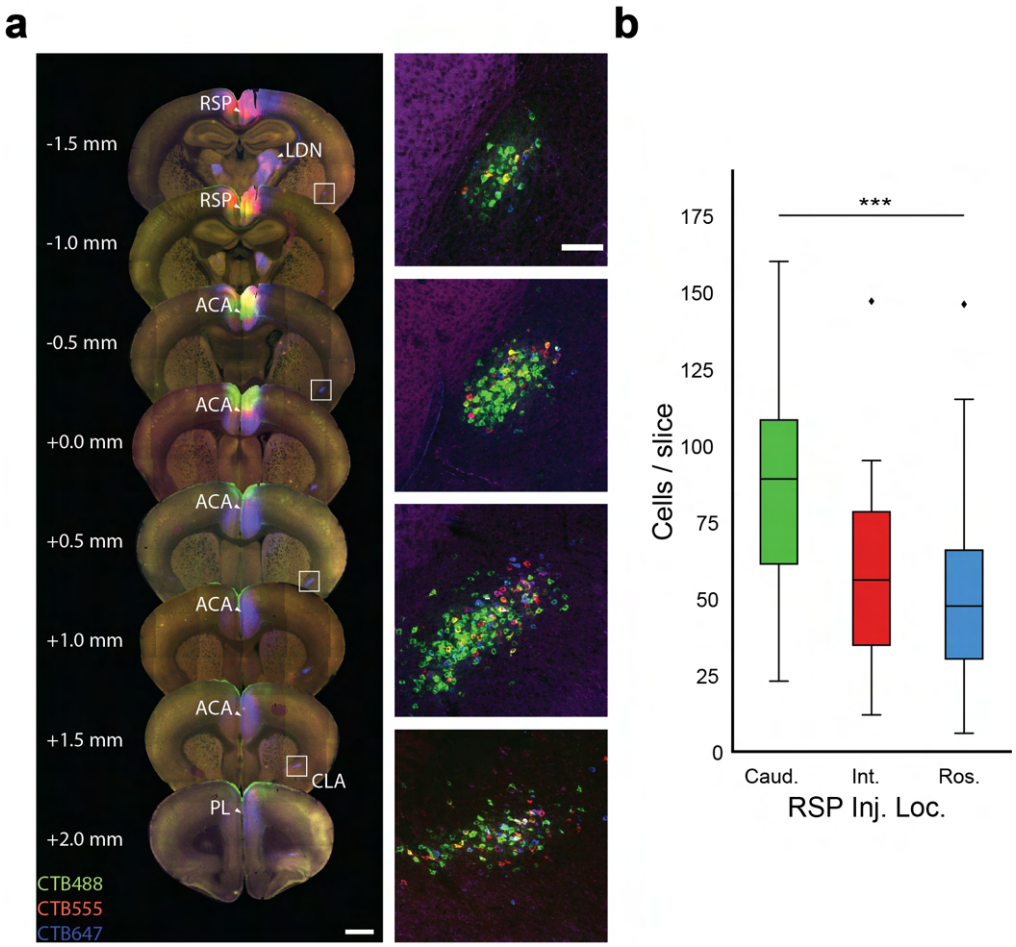

Supp. Fig. S 1. Triple CTB injections into RSP. **(a, left)** Representative sections spanning the rostrocaudal axis of the brain in which CLA neurons were retrogradely labeled with CTB from three different injection locations along the RSP (blue: rostral RSP, red: intermediate RSP, green: caudal RSP). **(a, right)** Insets of CLA from sections in a, left at 10X magnification. **(b)** Overall, caudal RSP injections yielded a higher penetrance of CLA neurons on a per slice basis.

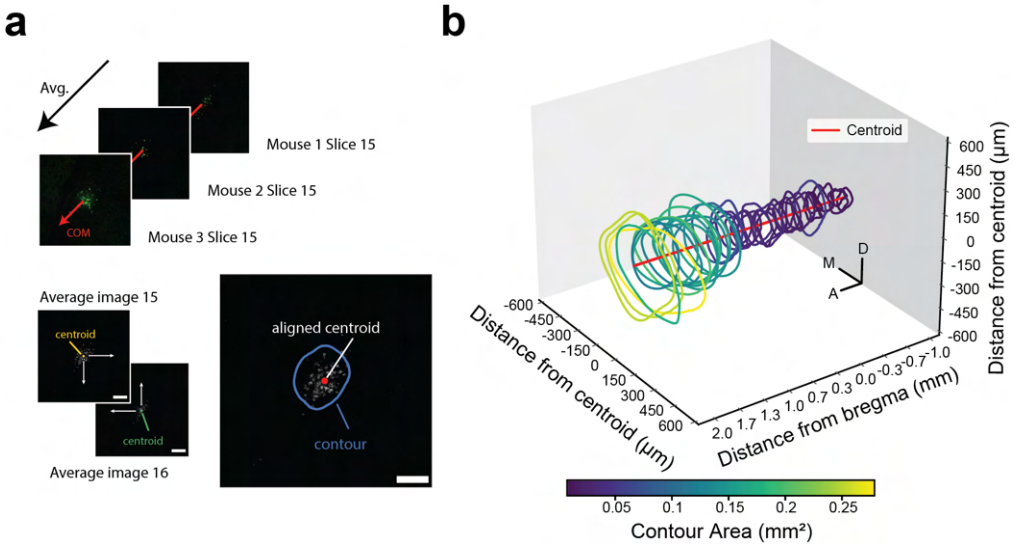

Supp. Fig. S 2. Modeling the spatial distribution of CLA_{RSP}. **(a)** Summary of processing steps for confocal images of the CLA (n = 3 mice). Slice images across mice were centroid-aligned and averaged for each matched slice. Active contours were initialized using an ellipse about the centroid and computed for each image. **(b)** 3D representation of contours of CLA_{RSP} neurons, rostral at left, colored by contour area. CLA contours are center-aligned and do not match anatomical position.

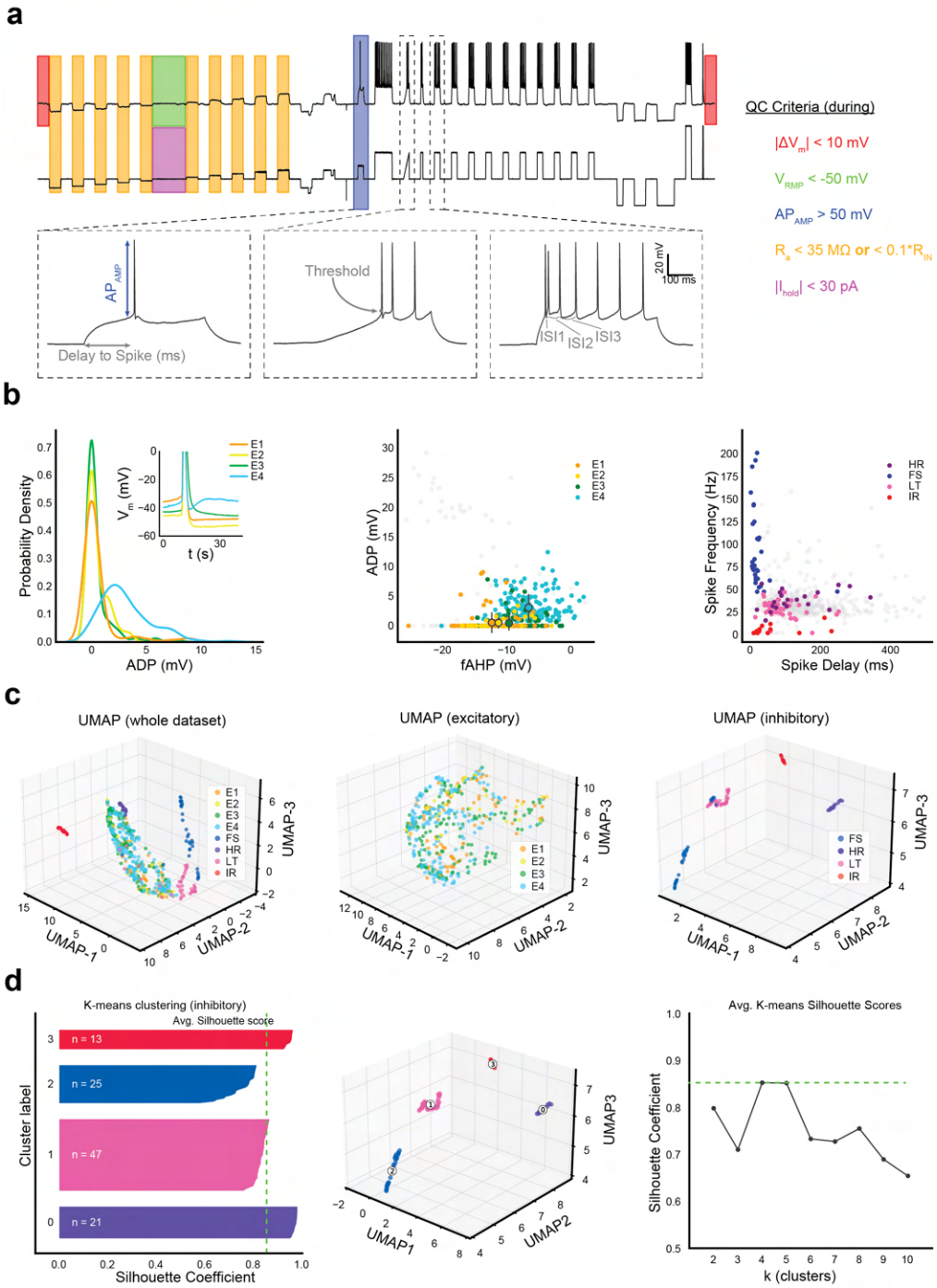

Supp. Fig. S 3. Dimensionality reduction and clustering of electrophysiological cell types. **(a)** Example standardized intrinsic electrophysiological trace overlaid with sections from which quality criteria values (right) are computed. **(b)** Comparisons of features within excitatory and inhibitory cell types. **(c)** UMAP dimensionality reduction of all cells (left), excitatory neurons (middle), and interneurons (right). Colors indicate cell type labels assigned during manual sorting. **(d)** Silhouette analysis of K-means clustering on UMAP of the interneuron class of CLA neurons. (left) Silhouette scores for each group in k = 4 clusters show a relatively high average separation. (middle) Projection of k-means cluster labels onto UMAP space. Note the similarity to (**c**, right). (right) Average silhouette scores for $2 \leqslant k \leqslant 10$ clusters. The similarity in 4 and 5 clusters appeared due to variability within the FS subclass.

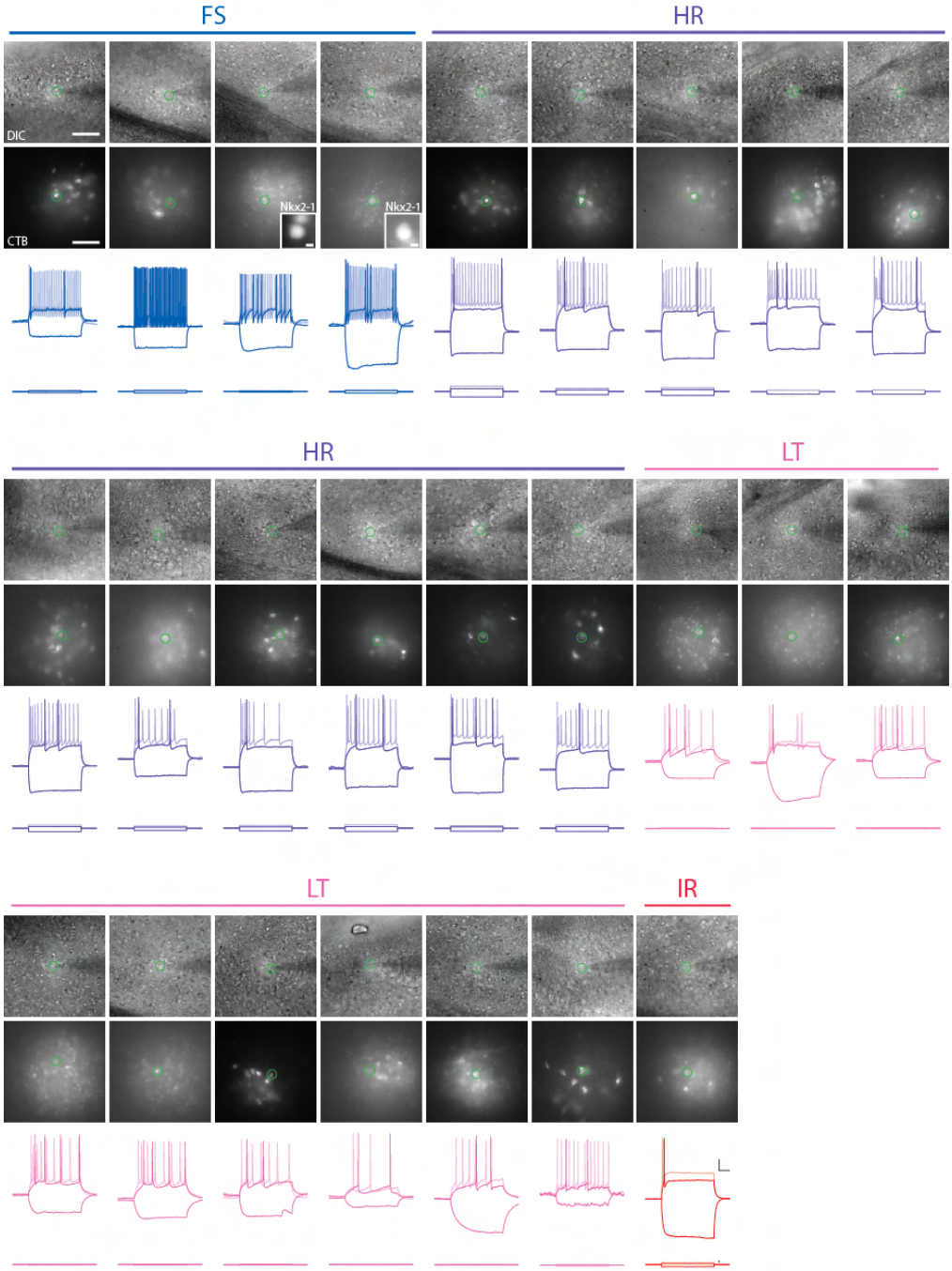

Supp. Fig. S 4. Projection interneurons span electrophysiological types. All CTB+ interneurons encountered during in vitro whole-cell patch-clamp experiments, arranged by type. In two experiments, we recorded from Nkx2.1-Cre;Ai9+ animals, finding two CTB+ FS interneurons co-labeled with tdTomato.

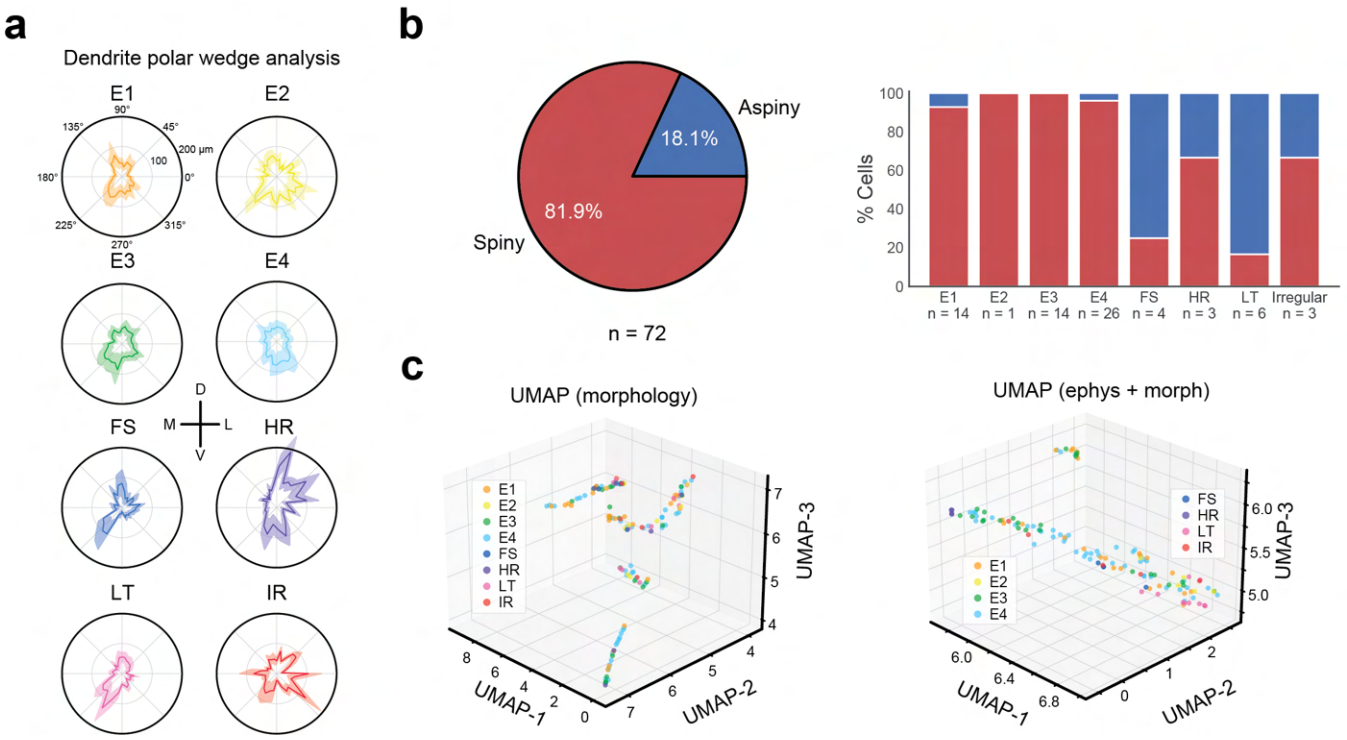

Supp. Fig. S 5. Dimensionality reduction and clustering the morphological dataset. **(a)** Morphological analysis of n = 134 reconstruction of CLA neurons. Average polar histograms of CLA neurons by type centered on the soma. **(b, left)** Analysis of spine counts from primary and secondary dendrites across the morphological dataset. **(b, right)** Percent of spiny vs. aspiny neurons sorted by electrophysiological type for neurons for which spine counts were possible (n = 72 cells). **(c, left)** UMAP dimensionality reduction of the morphological dataset alone, overlaid with electrophysiological cell type labels. **(c, right)** UMAP on the combined electrophysiological and morphological datasets.

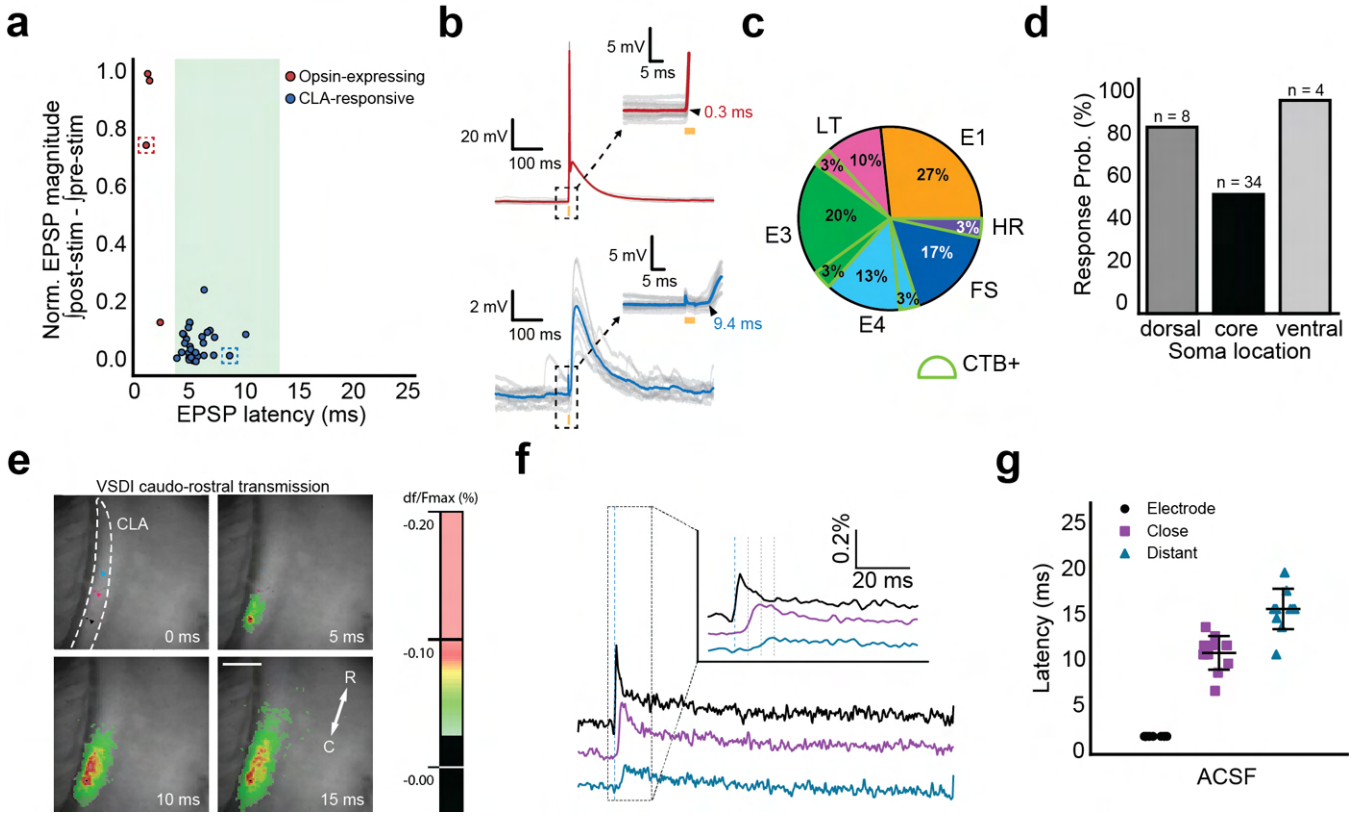

Supp. Fig. S 6. Intraclaustral signaling is monosynaptic and glutamatergic. **(a)** Normalized EPSP magnitude and onset latency for intraclaustral-responsive neurons. Neurons directly expressing opsin had larger and faster light-driven responses compared to monosynaptically connected neurons. Shaded region indicates window of monosynaptic latencies. **(b)** Example stimulus-evoked responses from neurons corresponding to the data points highlighted with dashed boxes in **a**. Insets demonstrate the differences in response latencies between opsin-expressing and CLA_{RSP}-responsive CLA neurons. **(c)** Among responsive neurons of all types, CTB+ neurons made up a small proportion. **(d)** Response probability for n = 46 neurons based on their dorsoventral location relative to CLA_{RSP} during patching. Neurons were less likely to respond if they occupied the CLA_{RSP} core. **(e)** VSDI experiments as in Fig. 3h-j with the stimulating electrode located in the caudal CLA. Scale bar = 1 mm. **(f)** Responses from representative pixels in **e**. **(g)** Quantification of f showing caudal-to-rostral delays in transmission from the stimulating electrode.

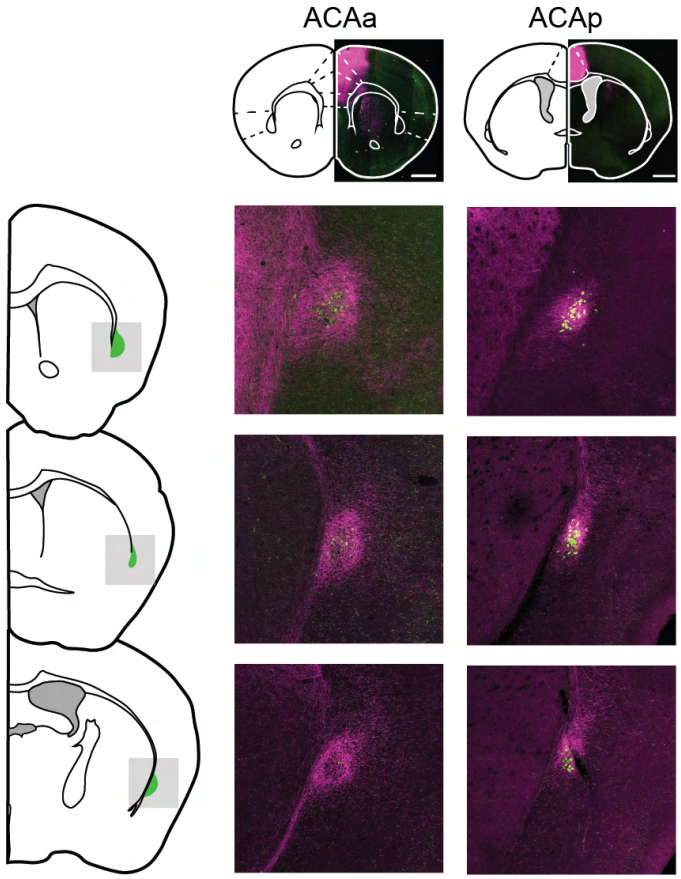

Supp. Fig. S 7. Histology from posterior ACA (ACAp) injections relative to anterior ACA (ACAa; n = 3 mice per injection site). Note the ventral projections and ring-like appearance in ACAa corticoclaustral projections.

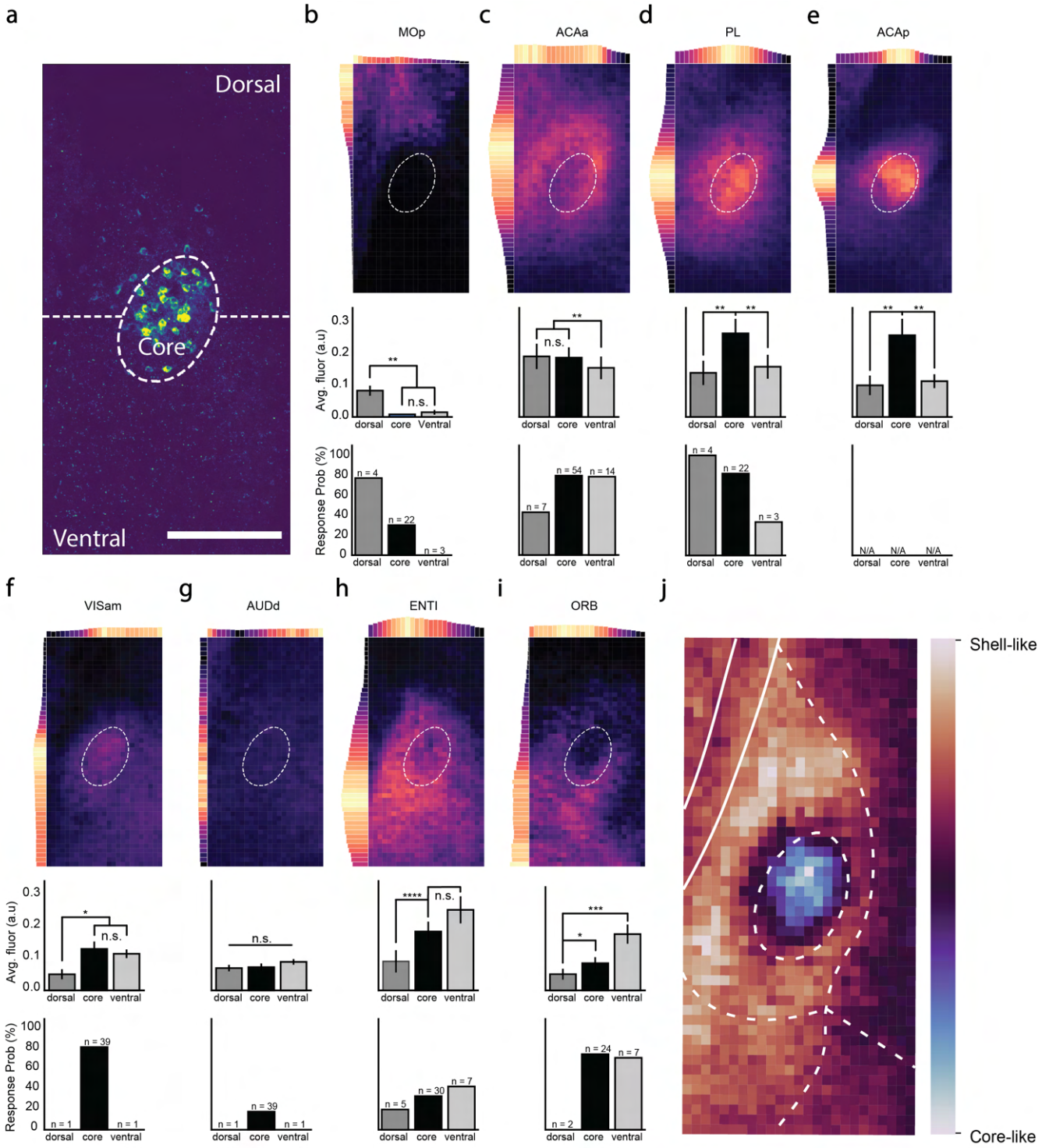

Supp. Fig. S 8. Analysis of cortical axon fluorescence and CLA neuron response probability. **(a)** Overlay of image masks (dorsal, core, ventral) used in subsequent analysis. **(b-i, top)** Average heat maps and histograms of fluorescence normalized to maximum signal along the dorsoventral and mediolateral axes for each injected cortical region (n = 3 mice per cortical area; dashed line is the average contour of CLA_{RSP} neurons from all experiments). **(b-i, middle)** Comparison of fluorescence in each mask region for each cortical area. **(b-i, bottom)** Response probabilities of CLA neurons to input from cortical axons after a brief (4 ms) photostimulation of presynaptic terminals, split by soma location relative to CLA_{RSP} during patching. **(j)** On the basis that a cortical area primarily displayed fluorescence in one masked CLA region, "core" and "shell" labels were applied to areas that projected to the core and dorsal/ventral CLA, respectively. Heat maps from within-label areas were then averaged and subtracted from heat maps from the other label. Displayed here is an index of similarity of pixels in the CLA to the "core" or "shell".

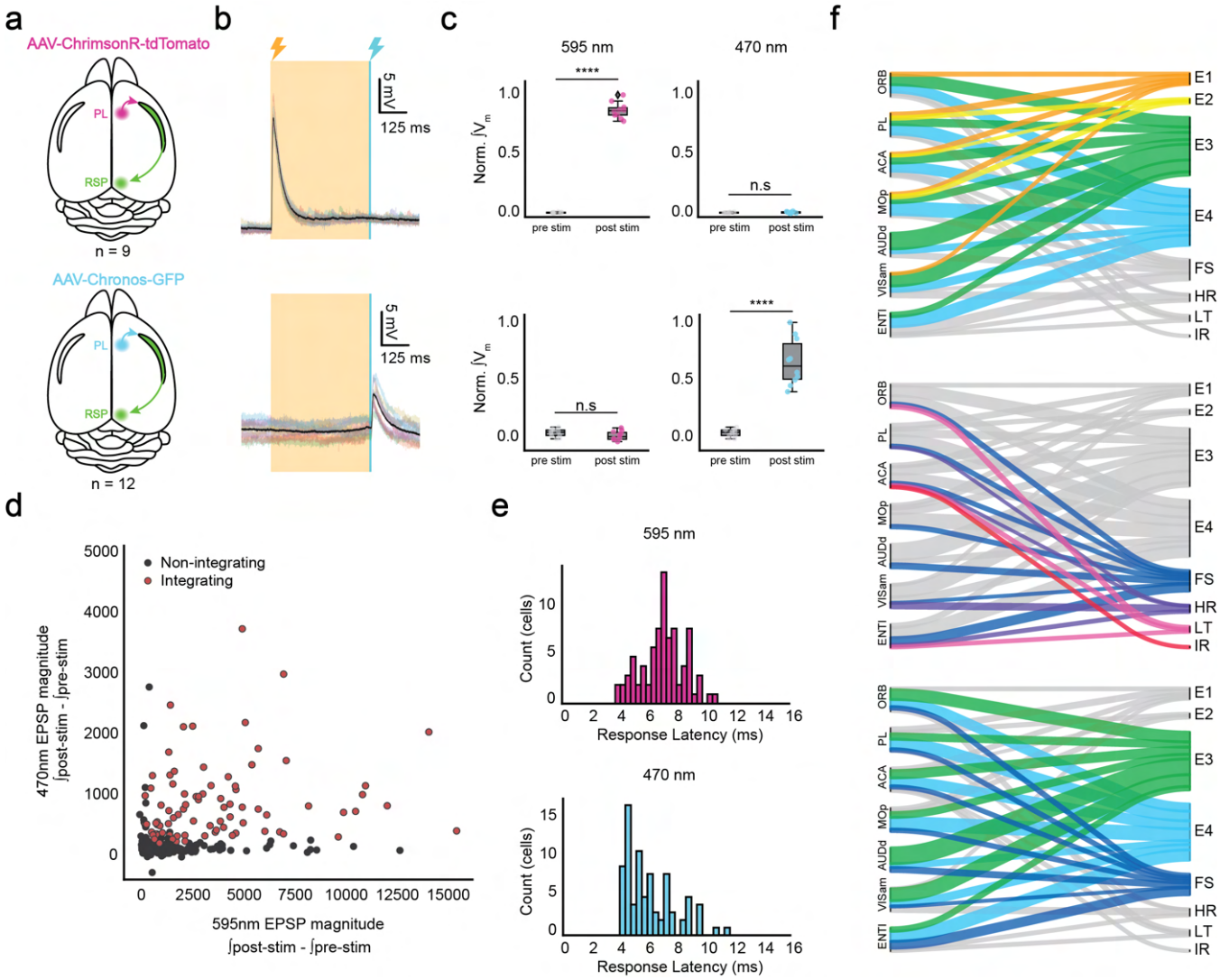

Supp. Fig. S 9. Sequential dual-color optogenetic stimulation eliminates optical cross-talk and reveals integrating responses and cortical connections in CLA neurons. **(a)** Schematics of control experiments of single-opsin injections into mPFC (n = 6 mice total, three each of Chrimson and Chronos injections). **(b)** Example traces of CLA neuron responses to cortical axon stimulation **(c)** Magnitude pre/post-stim comparisons of CLA EPSPs during sequential stimulation. Cross-talk in Chrimson-only experiments was effectively eliminated by extended exposure to 500 ms of 595 nm light. Responses to blue light photostimulation in Chronos-only experiments did not show cross-talk. **(d)** Magnitude responses to 470 nm and 595 nm light for all recorded cells (n = 259). Integrators displayed responses to both wavelengths (595: p = 6.1e-9, 470: p = 1.7e-10, Mann Whitney U test). **(e)** Latency of EPSPs in integrating postsynaptic neurons was within the typical monosynaptic range. Onset of Chronos EPSPs was typically faster than Chrimson. **(f)** River plots displaying different sets of cell types and the proportion of cortical inputs allocated to each type.

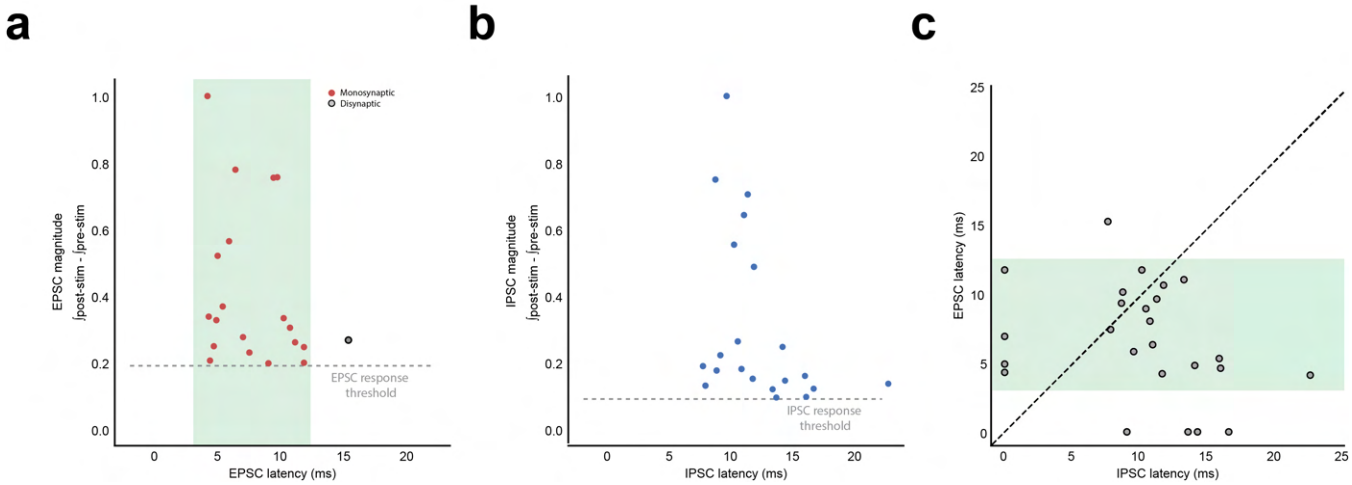

Supp. Fig. S 10. Photostimulation of monosynaptic CLA afferents in cortex. **(a)** EPSC magnitude and latencies among cortical neurons in response to CLA axon stimulation. **(b)** IPSC magnitude and latencies among cortical neurons. **(c)** EPSC and IPSC latency in all patched cortical neurons. Non-responsive neurons were given a latency of 0 ms for analytical and plotting convenience.

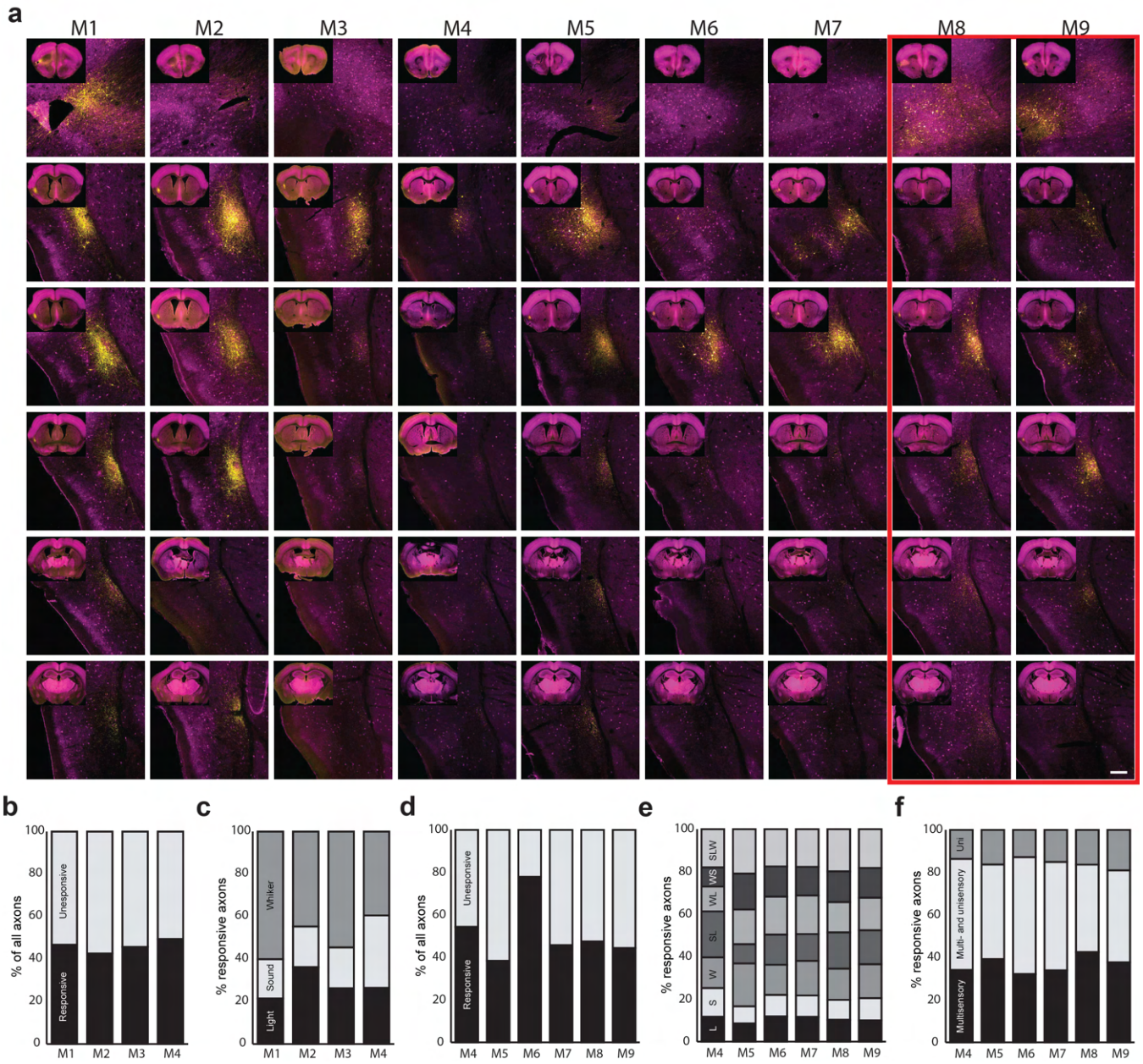

Supp. Fig. S 11. Expression of GCaMP7s localized to CLA neurons. **(a)** Representative high and low magnification (inset) images of sections spanning the rostrocaudal axis of the brain from mice (M1–9) used for calcium imaging. Sections were stained for parvalbumin (magenta) and GFP (yellow). Red rectangle indicates animals excluded from further analysis. Scale bar 200 μm. **(b)** Percentage of all recorded axons from each mouse in the unimodal data set displaying significant responses to one or more of the stimuli. **(c)** Percentage of all significantly activated axons from each mouse in the unimodal data set responsive to each stimulus type. **(d)** Percentage of all recorded axons from each mouse in the multimodal data set displaying significant responses to one or more of the stimuli. **(e)** Percentage of all significantly activated axons from each mouse in the multimodal data set responsive to each stimulus type. **(f)** Percentage of responsive axons from each mouse in the multimodal data set tuned to multimodal stimuli only, multi- or unimodal stimuli, and unimodal stimuli only.

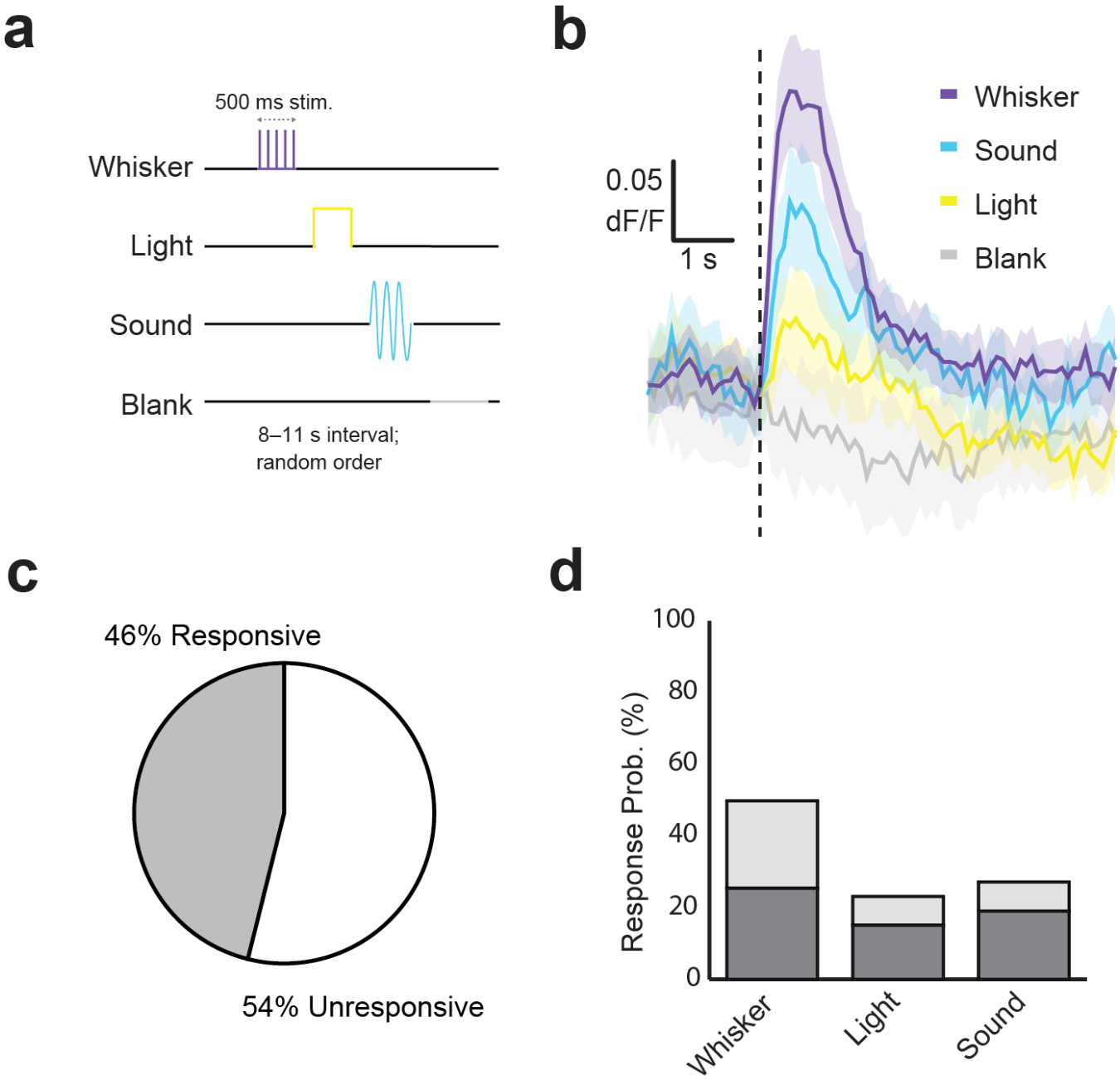

Supp. Fig. S 12. Recording calcium transients of CLA axons in cortex using unimodal sensory stimulation. **(a)** Passive stimulation protocol using three stimulus modalities. Stimuli were presented 8-11 s apart (randomized) with a "blank" period where no stimulus was presented every 4 trials. **(b)** Average dF/F traces for each stimulus across all axons responsive to that modality. **(c)** Percentage of all recorded axons displaying significant responses to one or more of the stimuli (n=4 mice, 1342 axons). **(d)** Percentage of all significantly activated axons responsive to each stimulus type. Light gray bars show the percentage exclusively responsive to each stimulus type.

Property	E1	E2	E3	E4	FS	HR	LT	IR
R_{in} (MΩ)	350 ± 136	401 ± 163	270 ± 112	310 ± 131	341 ± 189	110 ± 19	669 ± 298	231 ± 119
RMP (mV)	-70.1 ± 5.1	-67.4 ± 4.1	-70.6 ± 5.3	-70.5 ± 4.6	-66.0 ± 5.6	-75.4 ± 6.3	-66.5 ± 4.0	-69.7 ± 5.2
Thre. (mV)	-39.0 ± 5.4	-37.8 ± 4.8	-38.2 ± 5.0	-37.9 ± 4.1	-41.2 ± 7.6	-35.6 ± 3.8	-40.9 ± 5.6	-37.5 ± 5.5
Rheo. (pA)	79 ± 38	66 ± 35	109 ± 50	89 ± 42	97 ± 55	298 ± 65	36 ± 12	163 ± 96
fAHP (mV)	-12.3 ± 3.4	-11.3 ± 3.5	-9.6 ± 3.4	-6.5 ± 3.4	-18.2 ± 4.5	-9.3 ± 3.5	-13.2 ± 5.8	-8.7 ± 3.1
ADP (mV)	0.5 ± 1.7	0.5 ± 0.1	0.5 ± 1.19	3.1 ± 2.24	N/A	1.4 ± 2.2	N/A	N/A
$AP_{1/2}$ (ms)	1.8 ± 0.4	1.7 ± 0.2	1.9 ± 0.5	1.8 ± 0.5	0.8 ± 0.3	1.7 ± 0.4	1.7 ± 0.6	1.9 ± 0.6
Freq. (Hz)	38.9 ± 21.8	37.7 ± 12.4	33.2 ± 11.8	33.6 ± 13.5	93.2 ± 44.0	38.5 ± 10.8	28.8 ± 9.6	6.0 ± 4.9
AP_{max} (mV)	79.3 ± 9.2	68.2 ± 9.3	77.8 ± 9.9	74.9 ± 8.8	75.2 ± 11.8	81.8 ± 6.7	75.9 ± 9.2	83.0 ± 6.7
Spk_{delay} (ms)	188 ± 104	216 ± 106	152 ± 94	137 ± 68	24 ± 42	127 ± 87	99 ± 65	70 ± 75

Supp. Table. S 1. Select electrophysiological properties of CLA neurons. All values reported here as the mean ± the standard deviation. Abbreviations: R_{in} - input resistance, RMP - resting membrane potential, Thre. - spike threshold, Rheo. - rheobase current, fAHP - fast afterhyperpolarization potential, ADP - afterdepolarization potential, $AP_{1/2}$ - action potential half-width, Freq. - maximum recorded spike frequency, AP_{max} - maximum spike height at rheobase, Spk_{delay} - delay to spike onset.

Property	E1	E2	E3	E4	FS	HR	LT	IR
#Den.	5 ± 2	6 ± 3	5 ± 1	6 ± 2	4 ± 2	6 ± 1	4 ± 2	6 ± 2
#Nodes	14 ± 8	15 ± 8	20 ± 11	19 ± 12	12 ± 7	29 ± 15	11 ± 6	16 ± 11
<Den.> (μm)	349 ± 253	473 ± 294	368 ± 192	427 ± 328	314 ± 144	409 ± 157	416 ± 235	519 ± 521
Max $Den._{order}$	6 ± 2	8 ± 2	7 ± 2	7 ± 3	5 ± 2	9 ± 2	5 ± 1	7 ± 3
<Seg.> (μm)	50.3 ± 27.5	64.7 ± 23.0	43.0 ± 19.5	54.6 ± 18.1	46.5 ± 11.5	39.6 ± 6.5	68.1 ± 28.5	58.4 ± 20.7
ND (n/sholl)	3.7 ± 2.5	2.5 ± 1.5	5.3 ± 2.5	4.3 ± 2.7	3.0 ± 2.2	7.2 ± 5.5	2.4 ± 1.8	2.9 ± 1.9
$Den._{max}$ (μm)	203 ± 129	298 ± 101	186 ± 99	236 ± 102	187 ± 76	210 ± 116	279 ± 126	284 ± 134
$Len._{max}$ (°)	20 ± 79	50 ± 94	10 ± 100	10 ± 100	0 ± 120	40 ± 60	340 ± 110	0 ± 120

Supp. Table. S 2. Select morphological properties of CLA neurons. All values reported here as the mean ± the standard deviation. Abbreviations: #Den. - number of primary dendrites, #Nodes - number of dendritic nodes, <Den.> - average dendritic length, Max $Den._{order}$ - the highest order dendrite, <Seg.> - average dendritic segment length, ND - node density, $Den._{max}$ - longest dendrite, $Len._{max}$ - the polar bin of the longest dendrite.